Simply, linear correction could be applied to convert to the apparent k value as has been performed in this study. $CMRO_2$ values calculated using BM approach for the RW separation, were in good agreement with those determined with the direct measurement of RW as shown in Table 3.

The current method with modeling approach and simplified procedure provided consistent results in terms of time-dependent RW component, and consequently metabolic product of $^{15}O_2$ was separated from arterial whole blood for the $CMRO_2$ assessment in PET examination. The modeling approach to separate metabolite from authentic tracer has been showed previously for 6-[^{18}F]fluoro-L-dopa study (fdopa) (Huang *et al*, 1991). We expect that the modeling approach in conjunction with the simplified method showed in our study could be applied for various kinds of tracers, which require the separation of metabolic product such as fdopa. This approach enables us to assess parametric images for those tracers by eliminating the laborious procedures and by avoiding the amount of blood samplings, particularly for smaller animals.

In conclusion, the present RW model was feasible to reproduce RW TAC from a whole radioactivity concentration curve obtained after $^{15}O_2$ inhalation, and for a wide range of species. The simplified procedure to predict the RW TAC is of use to calculate $CMRO_2$ in smaller animals as well as clinical patients.

Acknowledgements

We acknowledge Mr N Ejima for operating the cyclotron and daily maintenance of CTI ECAT HR. We also gratefully thank Ms Atra Ardekani for her invaluable help on preparing the present paper. We also thank the staff of the Investigative Radiology, Research Institute, National Cardiovascular Center, especially, Dr T Inomata, Dr H Jino, Dr N Kawachi, and Dr T Zeniya for their assistance.

References

Aston JA, Cunningham VJ, Asselin MC, Hammers A, Evans AC, Gunn RN (2002) Positron emission tomography partial volume correction: estimation and algorithms. *J Cereb Blood Flow Metab* 22:1019–34

Eriksson L, Holte S, Bohm Chr, Kesselberg M, Hovander B (1988) Automated blood sampling system for positron emission tomography. *IEEE Trans Nucl Sci* 35:703–7

Eriksson L, Kanno I (1991) Blood sampling devices and measurements. *Med Prog Technol* 17:249–57

Fujita H, Kuwabara H, Reutens DC, Gjedde A (1999) Oxygen consumption of cerebral cortex fails to increase during continued vibrotactile stimulation. *J Cereb Blood Flow Metab* 19:266–71

Hayashi T, Watabe H, Kudomi N, Kim KM, Enmi J, Hayashida K, Iida H (2003) A theoretical model of oxygen delivery and metabolism for physiologic interpretation of quantitative cerebral blood flow and metabolic rate of oxygen. *J Cereb Blood Flow Metab* 23:1314–23

Hirano T, Minematsu K, Hasegawa Y, Tanaka Y, Hayashida K, Yamaguchi T (1994) Acetazolamide reactivity on ^{123}I-IMP single photon emission computed tomography in patients with major cerebral artery occlusive disease: correlation with positron emission tomography parameters. *J Cereb Blood Flow Metab* 14:763–70

Holden JE, Eriksson L, Roland PE, Stone-Elander S, Widen L, Kesselberg M (1988) Direct comparison of single-scan autoradiographic with multiple-scan least-squares fitting approaches to PET $CMRO_2$ estimation. *J Cereb Blood Flow Metab* 8:671–80

Huang SC, Barrio JR, Yu DC, Chen B, Grafton S, Melega WP, Hoffman JM, Satyamurthy N, Mazziotta JC, Phelps ME (1991) Modelling approach for separating blood time-activity curves in positron emission tomographic studies. *Phys Med Biol* 36:749–61

Iida H, Jones T, Miura S (1993) Modeling approach to eliminate the need to separate arterial plasma in oxygen-15 inhalation positron emission tomography. *J Nucl Med* 34:1333–40

Iida H, Kanno I, Miura S, Murakami M, Takahashi K, Uemura K (1989) A determination of the regional brain/blood partition coefficient of water using dynamic positron emission tomography. *J Cereb Blood Flow Metab* 9:874–85

Kaisti KK, Langsjo JW, Aalto S, Oikonen V, Sipila H, Teras M, Hinkka S, Metsahonkala L, Scheinin H (2003) Effects of sevoflurane, propofol, and adjunct nitrous oxide on regional cerebral blood flow, oxygen consumption, and blood volume in humans. *Anesthesiology* 99:603–13

Kudomi N, Choi C, Watabe H, Kim KM, Shidahara M, Ogawa M, Teramoto N, Sakamoto E, Iida H (2003) Development of a GSO detector assembly for a continuous blood sampling system. *IEEE Trans Nucl Sci* 50:70–3

Kudomi N, Hayashi T, Teramoto N, Watabe H, Kawachi N, Ohta Y, Kim KM, Iida H (2005) Rapid quantitative measurement of $CMRO_2$ and CBF by dual administration of ^{15}O-labeled oxygen and water during a single PET scan—a validation study and error analysis in anesthetized monkeys. *J Cereb Blood Flow Metab* 25:1209–24

Kudomi N, Watabe H, Hayashi T, Iida H (2007) Separation of input function for rapid measurement of quantitative $CMRO_2$ and CBF in a single PET scan with a dual tracer administration method. *Phys Med Biol* 52: 1893–908

Laforest R, Sharp TL, Engelbach JA, Fettig NM, Herrero P, Kim J, Lewis JS, Rowland DJ, Tai YC, Welch MJ (2005) Measurement of input functions in rodents: challenges and solutions. *Nucl Med Biol* 32:679–85

Lindstedt L, Schaeffer PJ (2002) Use of allometry in predicting anatomical and physiological parameters of mammals. *Lab Anim* 36:1–19

Magata Y, Temma T, Iida H, Ogawa M, Mukai T, Iida Y, Morimoto T, Konishi J, Saji H (2003) Development of injectable O-15 oxygen and estimation of rat OEF. *J Cereb Blood Flow Metab* 23:671–6

Meyer E, Tyler JL, Thompson CJ, Redies C, Diksic M, Hakim AM (1987) Estimation of cerebral oxygen utilization rate by single-bolus 15O2 inhalation and dynamic positron emission tomography. *J Cereb Blood Flow Metab* 7:403–14

Mintun MA, Raichle ME, Martin WR, Herscovitch P (1984) Brain oxygen utilization measured with O-15 radio-

tracers and positron emission tomography. *J Nucl Med* 25:177–87

Mintun MA, Vlassenko AG, Shulman GL, Snyder AZ (2002) Time-related increase of oxygen utilization in continuously activated human visual cortex. *Neuroimage* 16:531–7

Ohta S, Meyer E, Thompson CJ, Gjedde A (1992) Oxygen consumption of the living human brain measured after a single inhalation of positron emitting oxygen. *J Cereb Blood Flow Metab* 12:179–92

Okazawa H, Yamauchi H, Sugimoto K, Takahashi M, Toyoda H, Kishibe Y, Shio H (2001*a*) Quantitative comparison of the bolus and steady-state methods for measurement of cerebral perfusion and oxygen metabolism: positron emission tomography study using 15O-gas and water. *J Cereb Blood Flow Metab* 21:793–803

Okazawa H, Yamauchi H, Sugimoto K, Toyoda H, Kishibe Y, Takahashi M (2001*b*) Effects of acetazolamide on cerebral blood flow, blood volume, and oxygen metabolism: a positron emission tomography study with healthy volunteers. *J Cereb Blood Flow Metab* 21:1472–9

Pain F, Laniece P, Mastrippolito R, Gervais P, Hantraye P, Besret L (2004) Arterial input function measurement without blood sampling using a beta-microprobe in rats. *J Nucl Med* 45:1577–82

Sakoh M, Gjedde A (2003) Neuroprotection in hypothermia linked to redistribution of oxygen in brain. *Am J Physiol Heart Circ Physiol* 285:H17–25

Shidahara M, Watabe H, Kim KM, Oka H, Sago M, Hayashi T, Miyake Y, Ishida Y, Hayashida K, Nakamura T, Iida H (2002) Evaluation of a commercial PET tomograph-based system for the quantitative assessment of rCBF, rOEF and rCMRO2 by using sequential administration of 15O-labeled compounds. *Ann Nucl Med* 16:317–27

Temma T, Magata Y, Kuge Y, Shimonaka S, Sano K, Katada Y, Kawashima H, Mukai T, Watabe H, Iida H, Saji H (2006) Estimation of oxygen metabolism in a rat model of permanent ischemia using positron emission tomography with injectable^{15}O-O_2. *J Cereb Blood Flow Metab* 26:1577–83

Vafaee MS, Gjedde A (2000) Model of blood-brain transfer of oxygen explains nonlinear flow-metabolism coupling during stimulation of visual cortex. *J Cereb Blood Flow Metab* 20:747–54

Votaw JR, Shulman SD (1998) Performance evaluation of the Pico-Count flow-through detector for use in cerebral blood flow PET studies. *J Nucl Med* 39:509–15

Weber B, Burger C, Biro P, Buck A (2002) A femoral arteriovenous shunt facilitates arterial whole blood sampling in animals. *Eur J Nucl Med Mol Imaging* 29: 319–23

Wessen A, Widman M, Andersson J, Hartvig P, Valind S, Hetta J, Langstrom B (1997) A positron emission tomography study of cerebral blood flow and oxygen metabolism in healthy male volunteers anaesthetized with eltanolone. *Acta Anaesthesiol Scand* 41:1204–12

Yamauchi H, Okazawa H, Kishibe Y, Sugimoto K, Takahashi M (2003) The effect of acetazolamide on the changes of cerebral blood flow and oxygen metabolism during visual stimulation. *Neuroimage* 20:543–9

Yee SH, Lee K, Jerabek PA, Fox PT (2006) Quantitative measurement of oxygen metabolic rate in the rat brain using microPET imaging of briefly inhaled 15O-labelled oxygen gas. *Nucl Med Commun* 27:573–81

DOI: 10.3171/2009.9.JNS09345

Slowly progressive neuronal death associated with postischemic hyperperfusion in cortical laminar necrosis after high-flow bypass for a carotid intracavernous aneurysm

Case report

Koji Iihara, M.D., Ph.D., Masakazu Okawa, M.D., Tomohito Hishikawa, M.D., Ph.D., Naoaki Yamada, M.D., Ph.D., Kazuhito Fukushima, M.D., Ph.D., Hidehiro Iida, Ph.D., and Susumu Miyamoto, M.D., Ph.D.

Departments of Neurosurgery and Radiology, National Cardiovascular Center, Osaka, Japan

The authors report a rare case of slowly progressive neuronal death associated with postischemic hyperperfusion in cortical laminar necrosis after radial artery/external carotid artery–middle cerebral artery bypass graft surgery for an intracavernous carotid artery aneurysm. Under barbiturate protection, a 69-year-old man underwent high-flow bypass surgery combined with carotid artery sacrifice for a symptomatic intracavernous aneurysm. The patient became restless postoperatively, and this restlessness peaked on postoperative Day (POD) 7. Diffusion-weighted and FLAIR MR images obtained on PODs 1 and 7 revealed subtle cortical hyperintensity in the temporal cortex subjected to temporary occlusion. On POD 13, ^{123}I-iomazenil (^{123}I-IMZ) SPECT clearly showed increased distribution on the early image and mildly decreased binding on the delayed image with count ratios of the affected–unaffected corresponding regions of interest of 1.23 and 0.84, respectively, suggesting postischemic hyperperfusion. This was consistent with the finding on ^{123}I-iodoamphetamine SPECT. Of note, neuronal density in the affected cortex on the delayed ^{123}I-IMZ image further decreased to the affected/unaffected ratio of 0.44 on POD 55 during the subacute stage when characteristic cortical hyperintensity on T1-weighted MR imaging, typical of cortical laminar necrosis, was emerging. The affected cortex showed marked atrophy 8 months after the operation despite complete neurological recovery. This report illustrates, for the first time, dynamic neuroradiological correlations between slowly progressive neuronal death shown by ^{123}I-IMZ SPECT and cortical laminar necrosis on MR imaging in human stroke. *(DOI: 10.3171/2009.9.JNS09345)*

Key Words • **laminar necrosis** • **iomazenil** • **bypass** • **delayed neuronal death** • **magnetic resonance imaging**

Cortical laminar necrosis is a permanent brain injury radiologically characterized by T1-weighted MR imaging–documented high-intensity cortical lesions that follow the gyral anatomy of the cerebral cortex.[7,17,19] It has been associated with hypoxia, metabolic disturbances, drugs, infections, status epilepticus, and ischemic stroke.[7,19] The neuropathological correlations, however, between neuronal loss and an emerging cortical T1 hyperintensity signal in human stroke remain unknown. Intracavernous CA aneurysms are usually treated by trapping with/without EC-IC bypass based on presumed tolerance to CA sacrifice.[6,9] Flumazenil and iomazenil are markers of central benzodiazepine receptors, part of the GABAergic complex,[2] and are ideal markers of periinfarct tissue and incomplete brain infarcts.[16] This is the first report illustrating slowly progressive neuronal death, shown by ^{123}I-IMZ, during emerging cortical laminar necrosis on MR imaging after temporary occlusion at high-flow bypass for an intracavernous CA aneurysm.

Abbreviations used in this paper: CA = carotid artery; EC-IC = extracranial-intracranial; ECA = external carotid artery; ^{123}I-IMP = ^{123}I-iodoamphetamine; ^{123}I-IMZ = ^{123}I-iomazenil; MCA = middle cerebral artery; POD = postoperative day; RA = radial artery.

Case Report

History and Examination. This 69-year-old man developed double vision and ptosis due to left oculomotor palsy. Angiograms obtained at the previous hospital showed bilateral large intracavernous CA aneurysms (Fig. 1A). After balloon test occlusion showing intolerance on temporary occlusion of the left CA, the patient was referred to our institution.

Operation. The patient's left large CA aneurysm was trapped by RA/ECA-MCA bypass grafting without causing any neurological deficit. Temporary occlusion of the inferior trunk of M_2 was performed for 52 minutes under thiopental brain protection. Postoperative MR dif-

fusion weighted imaging demonstrated no abnormality. Two months later, the patient presented with contralateral oculomotor palsy due to progressive growth of the contralateral aneurysm. He underwent virtually the same operation, except with a shorter duration of temporary occlusion (47 minutes) and except for the observation that back flow from the distal M_2 was slower and dark when the distal clip was first declamped after anastomosis, suggesting that the territory of the recipient artery had been subjected to ischemic insult due to insufficient collateral flow.

Postoperative Course. The patient awoke from anesthesia relatively soon without apparent neurological deficit. Diffusion weighted and FLAIR imaging on POD 1 showed slight cortical hyperintensity in the right temporal region (Fig. 1C and D). Angiograms obtained on POD 5 showed no opacification of the aneurysm and good bypass patency, but the patient gradually became restless. Diffusion weighted and FLAIR imaging repeated on POD 7 revealed similar findings (Fig. 1E and F). Because the signal change on diffusion weighted imaging, however, remained subtle, the cause of such MR imaging abnormality remained uncertain. Subtle Gd enhancement was noted in the temporal cortex. On POD 18, ^{123}I-IMZ SPECT showed increased distribution on the early image (15 minutes) and decreased binding on the delayed image (3 hours) in the temporal region corresponding to the hyperintensity area on diffusion weighted and FLAIR images (Fig. 2). Because early and delayed images of ^{123}I-IMZ SPECT represent the cerebral perfusion state and neuronal viability, respectively, these results clearly indicated that ischemic neuronal loss and postischemic hyperperfusion occurred as a result of ischemic insult by temporary occlusion during bypass surgery.

Chronological count ratio changes of the affected to the unaffected corresponding regions of interest on ^{123}I-IMZ and ^{123}I-IMP SPECT scans are shown in Fig. 3. In the temporal region subjected to temporary clipping, the affected/unaffected ratio on ^{123}I-IMZ scans decreased during the subacute period between PODs 18 (ratio 0.84) and 55 (ratio 0.44), and then it leveled off later (ratio 0.43 on POD 239), whereas it remained relatively constant in other regions. We did not obtain ^{123}I-IMZ SPECT scans before the operation. On ^{123}I-IMP SPECT, the affected/unaffected ratio transiently increased during PODs 13 (ratio 1.21) and 26 (ratio 1.23), and it progressively decreased on PODs 53 (ratio 0.84) and 236 (ratio 0.67) in the temporal region, although virtually no changes were noted in other areas.

Correlation of SPECT and MR Imaging Findings. Serial FLAIR images showed cortical hyperintensity, which appeared on POD 1, peaked during PODs 7 and 13, almost returned to normal on POD 56, and demonstrated atrophy in the right temporal lobe on POD 237 (Fig. 4). During transient hyperperfusion and chronic hypoperfusion stages, ^{123}I-iodoamphetamine FLAIR demonstrated marked cortical edema and chronic atrophic change of the affected region, respectively. Subtle diffusion weighted imaging hyperintensity in the affected area was shown between PODs 1 and 7 but disappeared on POD 35, despite slowly progressive neuronal death documented on ^{123}I-IMZ in the subacute phase (PODs 18–55), during which T1 cortical hyperintensity became prominent (PODs 35–56). The hyperperfusion state of the affected cortex was also confirmed by ^{123}I-IMP SPECT on POD 12. Hyperperfusion of the affected cortex gradually improved and returned to normal, as shown by ^{123}I-IMP SPECT on POD 53. Follow-up MR images showed unique chronological changes such that cortical hyperintensity of the affected cortex appeared on POD 35 and persisted at least until POD 56. Of note, cortical hyperintensity on FLAIR peaked on POD 7 and then gradually decreased in intensity and appeared almost normal on POD 56. In the late chronic stage on POD 237, cortical atrophy with secondary degeneration of the underlying subcortical white matter was noted. No hemorrhagic transformation was noted in the affected regions on CT scans throughout the observation period.

Follow-Up. The patient's cranial nerve III palsy and restlessness gradually improved and he resumed his previous lifestyle 5 months after the second surgery. Eight months after surgery, his Mini-Mental State Examination status returned to normal.

Discussion

We have presented, for the first time, dynamic neuropathological correlations between slowly progressive neuronal death during postischemic hyperperfusion, as shown on ^{123}I-IMZ and ^{123}I-IMP SPECT scans, and emerging cortical laminar necrosis, as shown on T1-weighted MR images, after RA/ECA-MCA bypass grafting for an intracavernous CA aneurysm.

Intracavernous CA aneurysms are usually treated by trapping with/without EC-IC bypass based on presumed tolerance to CA sacrifice.[9] If the CA does not tolerate the balloon test occlusion, a high-flow bypass is indicated when CA sacrifice is performed. Creation of an RA/ECA-MCA bypass graft is a common method of high-flow bypass, and the technical standards and pitfalls have been reported previously.[9,12] The incidence of ischemic complications has been reported to be ~ 10%[9] as a result of early graft occlusion and other causes, but the underlying etiological force, most of which has been considered thromboembolic, remains unproven in most cases.[6,9]

Cortical laminar necrosis is a permanent brain injury characterized on T1-weighted MR images by high-intensity cortical lesions that follow the gyral anatomy of the cerebral cortex. Histopathological and experimental animal studies have demonstrated much more vulnerability of the gray matter than white matter to ischemic necrosis due to hypoperfusion.[19] Previous studies have reported characteristic MR imaging findings of cortical laminar necrosis caused by hypoxic or ischemic brain damage.[7,19] Cortical enhancement on postcontrast T1-weighted images in the subacute stage, suggesting breakdown of the blood-brain barrier, and hyperintense cortical lesions on unenhanced T1-weighted images during the late subacute and early chronic stages were reported to be distributed in the laminae. Cortical laminar necrosis is usually reported

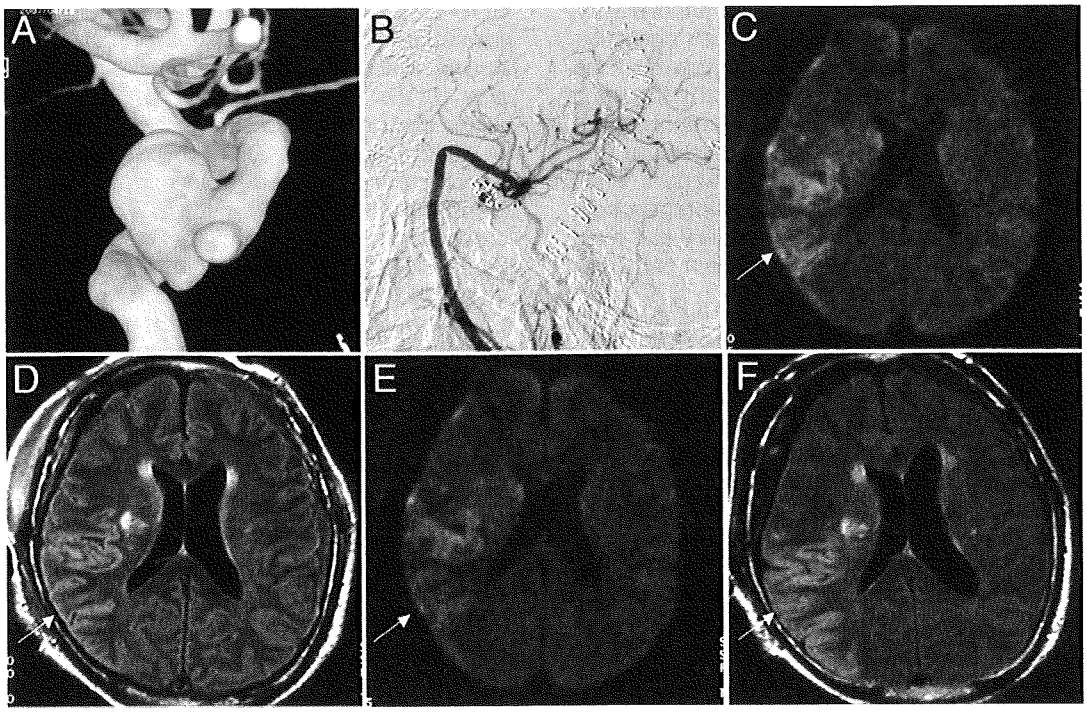

FIG. 1. **A:** Three-dimensional rotational CA angiogram showing a large intracavernous aneurysm that was treated with radial artery/ECA-MCA bypass grafting. **B:** Postoperative angiogram. **C and D:** Diffusion weighted **(C)** and FLAIR **(D)** images obtained on POD 1, showing only subtle hyperintensity in the right temporal cortex subjected to temporary clipping. **E and F:** Diffusion weighted **(E)** and FLAIR **(F)** images obtained on POD 7 when the patient became restless. Both of the hyperintensities following a gyral pattern appear slightly increased and well demarcated. *Arrows* indicate the affected region in the temporal lobe.

to be associated with volume loss of the affected cortex in the chronic stage.[20] Weiller and coworkers[20] have reported finding atrophy of the opercular cortex overlying the subcortical infarct on follow-up MR images ~ 1 year after the insult, suggesting that neuronal loss progresses over time.[13,20] In the present case we observed similar chronological changes of MR imaging signals on T1-weighted and FLAIR images and clearly illustrated the dynamic process of slowly progressive neuronal death associated with postischemic hyperperfusion in the affected cortex, where cortical hyperintensity was emerging in the subacute phase, following subtle diffusion weighted imaging–documented abnormalities in the acute phase.

Hyperperfusion is defined as a significant increase in cerebral blood flow relative to the homologous area of the contralateral hemisphere,[10] and it is known to occur after carotid endarterectomy, EC-IC bypass, and giant aneurysm clipping in patients with chronically impaired cerebrovascular reserve. Previous studies that involved the use of PET or SPECT scanning suggest that hyperperfusion may sometimes be associated with incomplete infarction or selective neuronal loss.[3,13] Flumazenil and ^{123}I-IMZ are markers of central benzodiazepine receptors, part of the GABAergic complex,[2] and ideal markers of periinfarct tissue and incomplete brain infarcts.[16] Sette et al.[16] have reported marked hyperperfusion in the affected territory in ischemic stroke, together with mildly reduced binding of ^{11}C-flumazenil in the acute stage, followed by reduced ^{11}C-flumazenil binding and reduced cerebral metabolic rates of glucose despite unaltered MR imaging findings in the subacute stage. Nakagawara and colleagues[13] have also reported using ^{123}I-IMZ SPECT in 2 patients with extensive hyperperfusion in the acute stage who exhibited reduced binding of ^{123}I-iomazenil in these areas in the chronic stage despite normal CT findings. The degree and duration of moderate ischemia in the present case was probably in the narrow range, which caused slowly progressive neuronal death without the development of frank infarction involving subcortical white matter, as reported in transient ischemia in animal models.[1] In internal carotid artery occlusive disease, selective neuronal damage was reported to occur beyond the regions of infarcts by hemodynamic ischemia in the chronic stage, as demonstrated on ^{11}C-flumazenil PET scans.[22]

The diagnostic significance of diffusion weighted imaging deserves some mention. Diffusion weighted imaging is considered an accurate predictor of the extent of infarction during the acute or early subacute phase of cerebral ischemia. Heiss et al.[4] compared the probability of cortical infarction by examining flumazenil binding on PET and diffusion weighted images in early ischemic stroke; they concluded that these modalities are comparable in predicting the probability of ischemic cortical infarction. Benzodiazepine receptor activity is a reliable marker of neuronal integrity in the cortex, but movement of water molecules in the extracellular space may be a more variable indicator of tissue damage, such that the false-positive volumes not included in the final infarct were larger for diffusion weighted imaging.[4] Subtle cortical hyperintensity on diffusion weighted imaging of the

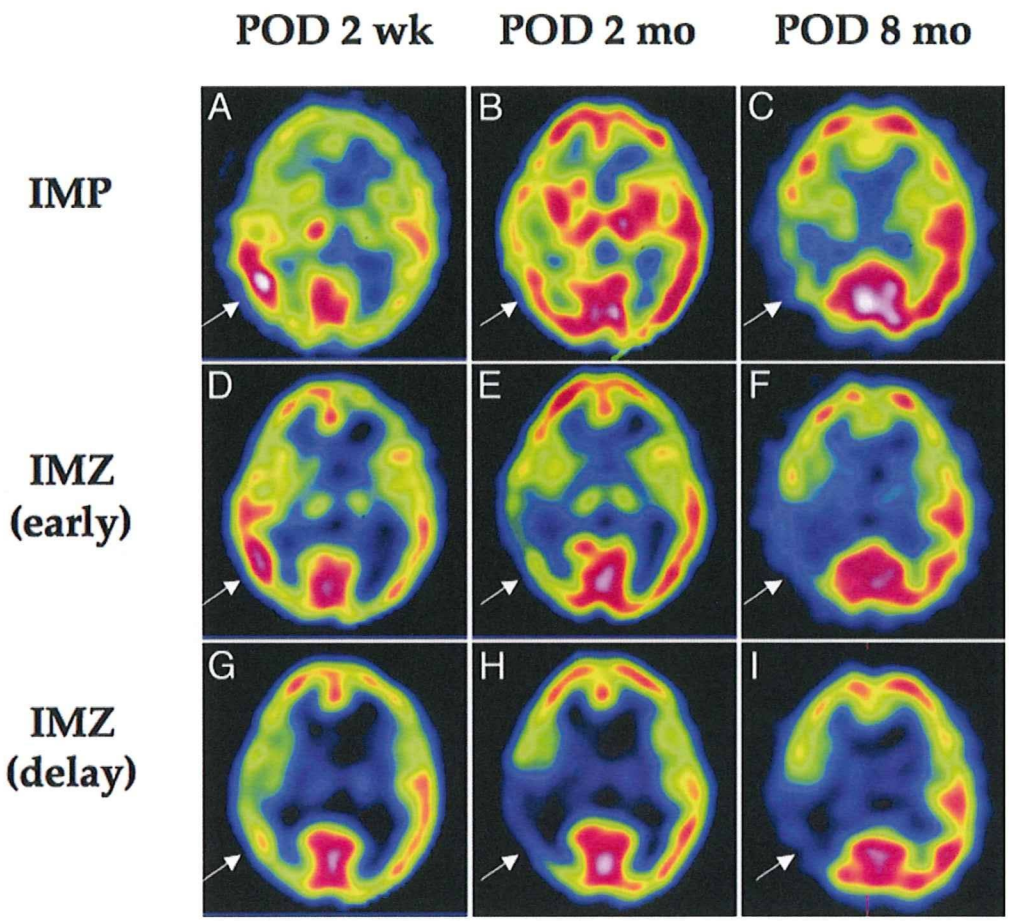

Fig. 2. Chronological changes in ^{123}I-IMP and early and delayed ^{123}I-IMZ SPECT images. Iodine-123–labeled iodoamphetamine **(A–C)** and early ^{123}I-IMZ **(D–F)** images similarly showing a transient increase in the subacute stage (POD 2 weeks [POD 2 wk; **A and D**]), followed by progressive decrease in the early and late chronic stages (POD 2 months [POD 2 mo; **B and E**] and 8 months [POD 8 mo; **C and F**]) of uptake in the affected regions. Delayed images of ^{123}I-IMZ **(G–I)** demonstrating delayed decrease of binding of the affected regions between subacute **(G)** and early chronic **(H)** stages, which levels off in the late chronic stage **(I)**. *Arrows* indicate the affected region in the temporal lobe.

affected cortex on PODs 1 and 7 in this case, as reported in global ischemia,[11] disappeared thereafter, despite ongoing neuronal loss during the subacute stage. In animal models, modest signal intensity changes on diffusion weighted imaging precede delayed neuronal necrosis after transient ischemia.[15] In the present case, however, the rate of decrease of the affected/unaffected ratio, as seen on the delayed ^{123}I-IMZ images, remained constant until POD 55 before and after the first postoperative ^{123}I-IMZ image, if the affected/unaffected ratio before surgery in

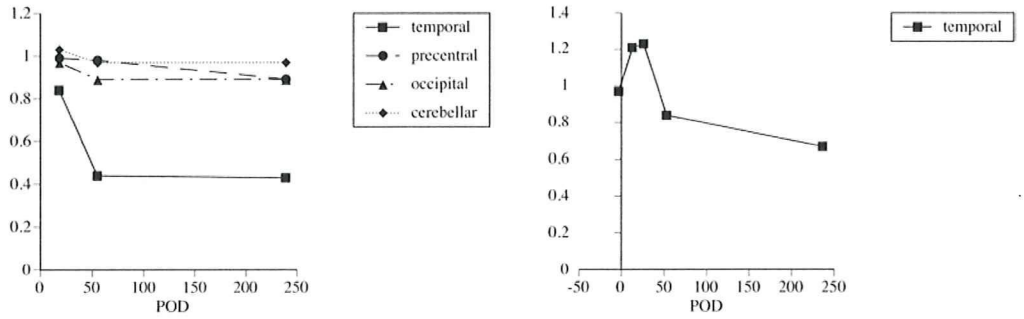

Fig. 3. Line graphs depicting chronological changes of the affected/unaffected count ratio and corresponding regions of interest on delayed ^{123}I-IMZ ***(left)*** and ^{123}I-IMP ***(right)*** SPECT images. The count ratio of the affected/unaffected corresponding regions of interest of ^{123}I-IMZ in the different areas (temporal, precentral, occipital, and cerebellar regions) are plotted against PODs. The affected/unaffected ratio of ^{123}I-IMP was plotted only for the affected temporal region.

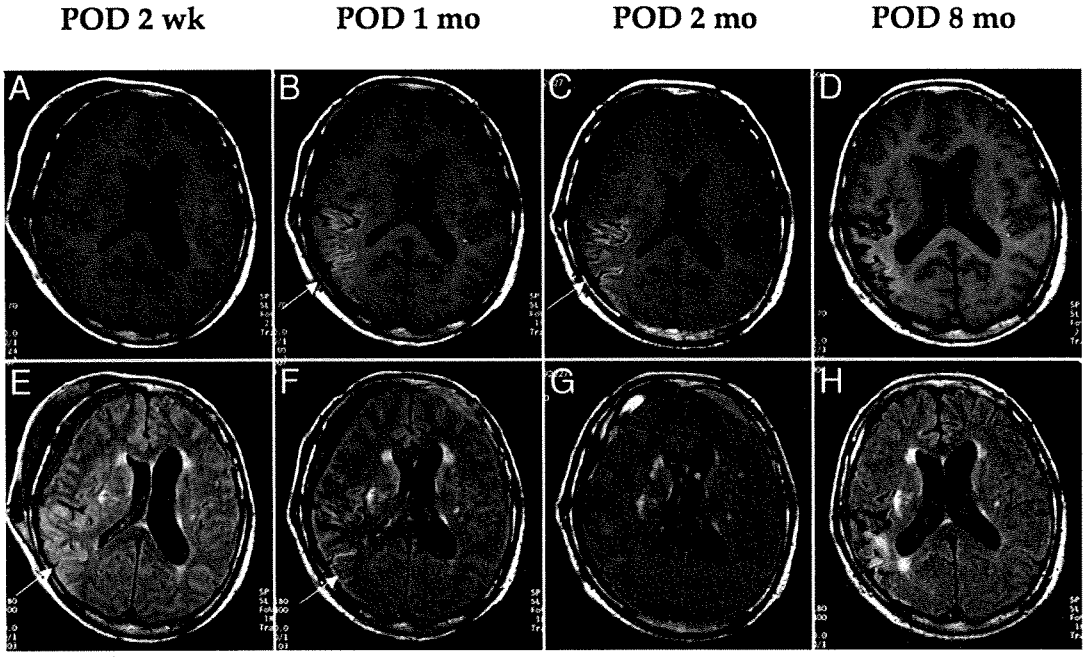

FIG. 4. Chronological changes demonstrated on follow-up MR images. Sagittal T1-weighted images (**A–D**) showing emerging cortical hyperintensity of the affected cortex between 2 weeks after surgery (POD 2 wk; **A**) and 1 month after surgery (POD 1 mo; **B**); the hyperintensity becomes more prominent at 2 months (POD 2 mo; **C**). Cortical laminar necrosis indicates atrophic change in the late chronic stage (**D**). **E–H:** On FLAIR images, cortical hyperintensity gradually decreases from 2 weeks after surgery (POS 2 wk; **E**) to 1 month after surgery (POD 1 mo; **F**) postoperatively and almost disappears by 2 months (POD 2 mo; **G**). In the late chronic stage, cortical atrophy with secondary degeneration of the underlying subcortical white matter is noted (**H**).

the affected cortex was assumed to be 1.0, as in the other areas on the first postoperative ^{123}I-IMZ image. These findings suggest that neuronal loss may not be of delayed onset, but rather slowly progressive after surgery, and diffusion weighted and ^{123}I-IMZ imaging may differ in predicting the probability of slowly progressive neuronal death in cortical laminar necrosis, depending on the interval from the moderate ischemic insult. Iodine-123–labeled IMZ SPECT is useful for examining the dynamic process of slowly progressive neuronal loss, especially in the subacute phase after moderate ischemia. Precise understanding of temporal profiles of neuronal death underlying emerging cortical laminar necrosis should require further accumulation of evidence using ^{123}I-IMZ SPECT.

Previous studies discussed the time permitted for temporary occlusion of the parent artery for aneurysm surgery, especially for an MCA bifurcation aneurysm.[8,12,14] In radial artery/ECA-MCA bypass grafting, however, the time permitted for temporary occlusion of the M_2 segment remains unclear, although the anastomotic time has been recommended to be less than 45 minutes.[12] Obviously, the time threshold for temporary occlusion may depend on multiple factors, such as the use of various neuroprotective agents,[8,14] brain temperature,[21] and extent of collateral flow and cerebrovascular reserve. During the previous 6 years, neither isolated cortical laminar necrosis nor frank infarction due to temporary occlusion had been documented in the other 21 cases treated by high-flow bypass, including 10 patients in whom temporary occlusion lasted more than 45 minutes. In the present case, extremely slow backflow from the distal side of the clamped artery was a key intraoperative finding, underlying the development of slowly progressive neuronal death. Although previous studies have reported possible preventative measures of ischemic complications related to temporary occlusion, such as excimer laser–assisted nonocclusive anastomosis,[18] the development of small intravascular shunts,[12] and double insurance bypass,[5] there are no widely accepted methods for this purpose.

Conclusions

We have discussed a rare case of slowly progressive neuronal death during postischemic hyperperfusion in cortical laminar necrosis associated with radial artery/ECA-MCA bypass grafting for intracavernous CA aneurysms. We have illustrated the diagnostic importance using of ^{123}I-IMZ SPECT in the subacute phase before emerging characteristic MR imaging findings. Moderate ischemia during temporary occlusion due to poor collateral flow may cause this rare ischemic complication.

Disclaimer

The authors report no conflict of interest concerning the materials or methods used in this study or the findings specified in this paper.

Acknowledgments

The authors thank Drs. Hiroshi Moriwaki, Kazuyuki Nagatsuka, and Kazunori Toyoda (Cerebrovascular Division, Department of Internal Medicine, National Cardiovascular Center); Masaki

Komiyama (Department of Neurosurgery, Osaka City General Hospital); and Shobu Namura (Department of Anatomy and Neurobiology, Morehouse School of Medicine) for helpful discussion, as well as Masaji Fukumoto (National Cardiovascular Center) for analyzing the data of ^{123}I-IMZ and ^{123}I-IMP SPECT.

References

1. Garcia JH, Liu KF, Ye ZR, Gutierrez JA: Incomplete infarct and delayed neuronal death after transient middle cerebral artery occlusion in rats. **Stroke 28:**2303–2310, 1997
2. Hantraye P, Kaijima M, Prenant C, Guibert B, Sastre J, Crouzel M, et al: Central type benzodiazepine binding sites: a positron emission tomography study in the baboon's brain. **Neurosci Lett 48:**115–120, 1984
3. Heiss WD, Grond M, Thiel A, Ghaemi M, Sobesky J, Rudolf J, et al: Permanent cortical damage detected by flumazenil positron emission tomography in acute stroke. **Stroke 29:**454–461, 1998
4. Heiss WD, Sobesky J, Smekal U, Kracht LW, Lehnhardt FG, Thiel A, et al: Probability of cortical infarction predicted by flumazenil binding and diffusion-weighted imaging signal intensity: a comparative positron emission tomography/magnetic resonance imaging study in early ischemic stroke. **Stroke 35:**1892–1898, 2004
5. Hongo K, Horiuchi T, Nitta J, Tanaka Y, Tada T, Kobayashi S: Double-insurance bypass for internal carotid artery aneurysm surgery. **Neurosurgery 52:**597–602, 2003
6. Jafar JJ, Russell SM, Woo HH: Treatment of giant intracranial aneurysms with saphenous vein extracranial-to-intracranial bypass grafting: indications, operative technique, and results in 29 patients. **Neurosurgery 51:**138–146, 2002
7. Komiyama M, Nakajima H, Nishikawa M, Yasui T: Serial MR observation of cortical laminar necrosis caused by brain infarction. **Neuroradiology 40:**771–777, 1998
8. Lavine SD, Masri LS, Levy ML, Giannotta SL: Temporary occlusion of the middle cerebral artery in intracranial aneurysm surgery: time limitation and advantage of brain protection. **J Neurosurg 87:**817–824, 1997
9. Lawton MT, Hamilton MG, Morcos JJ, Spetzler RF: Revascularization and aneurysm surgery: current techniques, indications, and outcome. **Neurosurgery 38:**83–84, 1996
10. Marchal G, Young AR, Baron JC: Early postischemic hyperperfusion: pathophysiologic insights from positron emission tomography. **J Cereb Blood Flow Metab 19:**467–482, 1999
11. McKinney AM, Teksam M, Felice R, Casey SO, Cranford R, Truwit CL, et al: Diffusion-weighted imaging in the setting of diffuse cortical laminar necrosis and hypoxic-ischemic encephalopathy. **AJNR Am J Neuroradiol 25:**1659–1665, 2004
12. Mohit AA, Sekhar LN, Natarajan SK, Britz GW, Ghodke B: High-flow bypass grafts in the management of complex intracranial aneurysms. **Neurosurgery 60 (2 Suppl 1):**ONS105–ONS123, 2007
13. Nakagawara J, Sperling B, Lassen NA: Incomplete brain infarction of reperfused cortex may be quantitated with iomazenil. **Stroke 28:**124–132, 1997
14. Ogilvy CS, Carter BS, Kaplan S, Rich C, Crowell RM: Temporary vessel occlusion for aneurysm surgery: risk factors for stroke in patients protected by induced hypothermia and hypertension and intravenous mannitol administration. **J Neurosurg 84:**785–791, 1996
15. Rojas S, Martin A, Justicia C, Falcon C, Bargallo N, Chamorro A, et al: Modest MRI signal intensity changes precede delayed cortical necrosis after transient focal ischemia in the rat. **Stroke 37:**1525–1532, 2006
16. Sette G, Baron JC, Young AR, Miyazawa H, Tillet I, Barre L, et al: In vivo mapping of brain benzodiazepine receptor changes by positron emission tomography after focal ischemia in the anesthetized baboon. **Stroke 24:**2046–2048, 1993
17. Siskas N, Lefkopoulos A, Ioannidis I, Charitandi A, Dimitriadis AS: Cortical laminar necrosis in brain infarcts: serial MRI. **Neuroradiology 45:**283–288, 2003
18. Streefkerk HJ, Bremmer JP, Tulleken CA: The ELANA technique: high flow revascularization of the brain. **Acta Neurochir Suppl 94:**143–148, 2005
19. Takahashi S, Higano S, Ishii K, Matsumoto K, Sakamoto K, Iwasaki Y, et al: Hypoxic brain damage: cortical laminar necrosis and delayed changes in white matter at sequential MR imaging. **Radiology 189:**449–456, 1993
20. Weiller C, Willmes K, Reiche W, Thron A, Isensee C, Buell U, et al: The case of aphasia or neglect after striatocapsular infarction. **Brain 116:**1509–1525, 1993
21. Westermaier T, Zausinger S, Baethmann A, Steiger HJ, Schmid-Elsaesser R: No additional neuroprotection provided by barbiturate-induced burst suppression under mild hypothermic conditions in rats subjected to reversible focal ischemia. **J Neurosurg 93:**835–844, 2000
22. Yamauchi H, Kudoh T, Kishibe Y, Iwasaki J, Kagawa S: Selective neuronal damage and borderzone infarction in carotid artery occlusive disease: a 11C-flumazenil PET study. **J Nucl Med 46:**1973–1979, 2005

Manuscript submitted March 2, 2009.
Accepted September 28, 2009.
Please include this information when citing this paper: published online October 30, 2009; DOI: 10.3171/2009.9.JNS09345.
Address correspondence to: Koji Iihara, M.D., Ph.D., Department of Neurosurgery, National Cardiovascular Center, 5-7-1 Fujishirodai, Suita, Osaka 565-8565, Japan. email: kiihara@hsp.ncvc.go.jp.

Ann Nucl Med
DOI 10.1007/s12149-009-0243-7

ORIGINAL ARTICLE

Influence of residual oxygen-15-labeled carbon monoxide radioactivity on cerebral blood flow and oxygen extraction fraction in a dual-tracer autoradiographic method

Katsuhiro Iwanishi · Hiroshi Watabe · Takuya Hayashi · Yoshinori Miyake · Kotaro Minato · Hidehiro Iida

Received: 14 December 2008 / Accepted: 8 January 2009

Abstract
Objective Cerebral blood flow (CBF), cerebral metabolic rate of oxygen ($CMRO_2$), oxygen extraction fraction (OEF), and cerebral blood volume (CBV) are quantitatively measured with PET with ^{15}O gases. Kudomi et al. developed a dual tracer autoradiographic (DARG) protocol that enables the duration of a PET study to be shortened by sequentially administrating $^{15}O_2$ and $C^{15}O_2$ gases. In this protocol, before the sequential PET scan with $^{15}O_2$ and $C^{15}O_2$ gases ($^{15}O_2$–$C^{15}O_2$ PET scan), a PET scan with $C^{15}O$ should be preceded to obtain CBV image. $C^{15}O$ has a high affinity for red blood cells and a very slow washout rate, and residual radioactivity from $C^{15}O$ might exist during a $^{15}O_2$–$C^{15}O_2$ PET scan. As the current DARG method assumes no residual $C^{15}O$ radioactivity before scanning, we performed computer simulations to evaluate the influence of the residual $C^{15}O$ radioactivity on the accuracy of measured CBF and OEF values with DARG method and also proposed a subtraction technique to minimize the error due to the residual $C^{15}O$ radioactivity.
Methods In the simulation, normal and ischemic conditions were considered. The $^{15}O_2$ and $C^{15}O_2$ PET count curves with the residual $C^{15}O$ PET counts were generated by the arterial input function with the residual $C^{15}O$ radioactivity. The amounts of residual $C^{15}O$ radioactivity were varied by changing the interval between the $C^{15}O$ PET scan and $^{15}O_2$–$C^{15}O_2$ PET scan, and the absolute inhaled radioactivity of the $C^{15}O$ gas. Using the simulated input functions and the PET counts, the CBF and OEF were computed by the DARG method. Furthermore, we evaluated a subtraction method that subtracts the influence of the $C^{15}O$ gas in the input function and PET counts.
Results Our simulations revealed that the CBF and OEF values were underestimated by the residual $C^{15}O$ radioactivity. The magnitude of this underestimation depended on the amount of $C^{15}O$ radioactivity and the physiological conditions. This underestimation was corrected by the subtraction method.
Conclusions This study showed the influence of $C^{15}O$ radioactivity in DARG protocol, and the magnitude of the influence was affected by several factors, such as the radioactivity of $C^{15}O$, and the physiological condition.

Keywords PET · OEF · CBV · Carbon monoxide

K. Iwanishi (✉) · H. Watabe · T. Hayashi · H. Iida
Department of Investigative Radiology, National Cardiovascular Center Research Institute, 5-7-1 Fujishirodai, Suita, Osaka 565-8565, Japan
e-mail: kiwanish@ri.ncvc.go.jp

Y. Miyake
Department of Radiology and Nuclear Medicine, National Cardiovascular Center, Osaka, Japan

K. Iwanishi · K. Minato
Infomatics Science, Nara Institute of Science and Technology, Nara, Japan

Introduction

Positron emission tomography with ^{15}O gas can quantitatively measure cerebral blood flow (CBF), oxygen extraction fraction (OEF), cerebral metabolic rate of oxygen ($CMRO_2$), and cerebral blood volume (CBV). These functional values are important clinical indices that can be used to evaluate ischemic degree mainly in chronic cerebral arterial occlusive diseases. Several quantitative approaches

Published online: 10 April 2009

have been developed to obtain CBF and $CMRO_2$ images based on a single-tissue compartment model for oxygen and water kinetics [1–4]. In the steady-state method [5–9], quantitative images are estimated from data acquired while in the steady state reached during the continuous inhalation of $^{15}O_2$ and $C^{15}O_2$. The study period with this method is long (approximately 2 h) due to the waiting time needed to reach equilibrium. The autoradiographic method, which uses separate administrations of three traces of CO, CO_2, and O_2 (three-step ARG), has also been employed [3, 10–14]. The study period with the ARG method is shorter than that need with the steady-state method. However, a study with the ARG method still takes more than half an hour, because there is a waiting time for the decay of the residual radioactivity of the preceding tracer used.

Previously, Kudomi et al. developed a dual tracer autoradiographic (DARG) method to shorten the PET study period [15, 16]. This method used a single PET scan with sequential administration of dual tracers of $^{15}O_2$ and $C^{15}O_2$ ($^{15}O_2$–$C^{15}O_2$ scan), and computed CBF and $CMRO_2$ simultaneously in an autoradiographic manner. Although the DARG approach eliminated the waiting time of radioactivity decay between $^{15}O_2$ and $C^{15}O_2$ administrations, a separate PET scan with $C^{15}O$ is required for obtaining a CBV image and correction of blood volume in $CMRO_2$ before the DARG scan. However, between these scans for $C^{15}O$ and the DARG we need another waiting time for the radioactivity decay of $C^{15}O$, since the DARG approach itself does not take into account the residual $C^{15}O$ radioactivity in the arterial input function (AIF) and PET data. Furthermore, CO has a relatively long biological clearance from the blood due to high affinity to hemoglobin. While it is desired to further decrease the waiting time for the decay in the actual clinical study, it has not been defined how long it should be, and how small amount of the residual activity will affect the accuracy of CBF and $CMRO_2$.

In this study, we performed computer simulations and evaluated the influence of this residual $C^{15}O$ radioactivity on the CBF and OEF values obtained by the DARG method. Moreover, we proposed a method to remove the influence of the $C^{15}O$ on the DARG method calculation (Subtraction method).

Materials and methods

Computation of functional values

CBF and OEF values were calculated from tissue TAC [$C_i(t)$] and AIF during an $^{15}O_2$–$C^{15}O_2$ scan, based on a single-tissue compartment model for oxygen and water, and the DARG method [15]. Using the method developed by Kudomi et al. [16], the AIF was separated into $^{15}O_2$ ($A_{O_2}(t)$) and $H_2^{15}O$ ($A_{H_2O}(t)$) (Note that although we used $C^{15}O_2$ gas, we used $H_2^{15}O$ for the expression in this section due to the rapid exchange of $H_2^{15}O$ by carbonate dehydratase in the lung). The total radioactivity in the tissue after the $^{15}O_2$ and $C^{15}O_2$ administration can be expressed as,

$$Ci(t) = f \cdot A_{H_2O}(t) \otimes \exp^{-\frac{f}{p}t} + E \cdot f \cdot A_{O_2}(t) \otimes \exp^{-\frac{f}{p}t} + V_B \cdot R_{Hct}(1 - Fv \cdot E) A_{O_2}(t) \quad (1)$$

where f is CBF, E is the OEF, p is the blood/tissue partition coefficient of water, R_{Hct} is the small-to-large vessel hematocrit ratio, and V_B is the cerebral blood volume. F_v is the effective venous fraction. The first term of the right-hand side describes the amount of water entering the tissue. The second term represents the amount of oxygen that enters the tissue and is immediately metabolized to water. The third term is the radioactivity of the $^{15}O_2$ in the blood vessels.

V_B is separately calculated using data from a $C^{15}O$ scan and the following equation [13]:

$$V_B = \frac{C_{CO}}{R_{Hct} \cdot \rho_{brain} \cdot RI_{CO} \cdot \rho_{blood}}. \quad (2)$$

ρ_{brain} and ρ_{blood} represent the densities of blood (=1.06 g/mL) and brain tissue (=1.04 g/mL). RI_{CO} (Bq/mL) is the mean of the radioactivity concentration for $C^{15}O$ in the arterial blood.

To calculate functional values using a look-up table procedure, Eq. 1 was integrated for the periods after the $H_2^{15}O$ (represents $\int_W$) and $^{15}O_2$ administration (represents $\int_O$) as

$$\begin{aligned}
\int_W Ci(t)dt &= f \int_W A_{H_2O}(t) \otimes \exp^{-\frac{f}{p}t} dt \\
&\quad + E \cdot f \int_W A_{O_2}(t) \otimes \exp^{-\frac{f}{p}t} dt + V_B \\
&\quad \cdot R_{Hct}(1 - Fv \cdot E) \int_W A_{O_2}(t)dt \\
\int_O Ci(t)dt &= f \int_O A_{H_2O}(t) \otimes \exp^{-\frac{f}{p}t} dt \\
&\quad + E \cdot f \int_O A_{O_2}(t) \otimes \exp^{-\frac{f}{p}t} dt + V_B \\
&\quad \cdot R_{Hct}(1 - Fv \cdot E) \int_O A_{O_2}(t)dt
\end{aligned} \quad (3)$$

From the above equation, E can be expressed as follows:

$$E = \frac{\int_o Ci(t) - f \int_o A_{H_2O} \otimes \exp^{-\frac{f}{p}t} dt - V_B \cdot R_{Hct} \int_o A_{O_2} dt}{f \int_o A_{O_2} \otimes \exp^{-\frac{f}{p}t} dt - V_B \cdot R_{Hct} \cdot Fv \int_o A_{O_2} dt}. \quad (4)$$

Substituting Eq. 4 into Eq. 3, we obtain

$$\int_w \mathrm{Ci}(t)\mathrm{d}t = f\int_w A_{\mathrm{H_2O}}(t)\otimes\exp^{\frac{-f}{p}t}\mathrm{d}t + V_{\mathrm{B}}\cdot R_{\mathrm{Hct}}\int_w A_{\mathrm{O_2}}(t)\mathrm{d}t + \left(f\int_w A_{\mathrm{O_2}}(t)\otimes\exp^{\frac{-f}{p}t}\mathrm{d}t - V_{\mathrm{B}}\cdot R_{\mathrm{Hct}}\cdot \mathrm{Fv}\int_w A_{\mathrm{O_2}}(t)\mathrm{d}t\right) \times \frac{\int_o \mathrm{Ci}(t) - f\int_o A_{\mathrm{H_2O}}\otimes\exp^{\frac{-f}{p}t}\mathrm{d}t - V_{\mathrm{B}}\cdot R_{\mathrm{Hct}}\int_o A_{\mathrm{O_2}}\mathrm{d}t}{f\int_o A_{\mathrm{O_2}}\otimes\exp^{\frac{-f}{p}t}\mathrm{d}t - V_{\mathrm{B}}\cdot R_{\mathrm{Hct}}\cdot \mathrm{Fv}\int_o A_{O_2}\mathrm{d}t}. \quad (5)$$

Using Eq. 5, f can be estimated using a look-up table procedure based on the integration value of the tissue TAC and separated input function. Next, E can be calculated using Eq. 4.

Study protocol with DARG method

Figure 1 shows a schematic diagram of the clinical study protocol with the DARG method for our institute. The PET scanner we used was an ECAT EXACT47 (CTI Inc., Knoxville, USA). First, a 10 min transmission scan was performed to correct for gamma ray attenuation. Then gaseous $C^{15}O$ of 2500 MBq was inhaled for 30 s, and 90 s post-inhalation, a 4 min emission scan ($C^{15}O$ scan) was performed to obtain a CBV image. Finally, a single dynamic PET scan was conducted during the sequential administration of gaseous $^{15}O_2$ (4000 MBq) and $C^{15}O_2$ (5000 MBq) in a short time interval. Their inhalation times were 1 min.

A catheter was inserted into the brachial artery of the patient. The arterial blood was sampled at the beginning of the $C^{15}O$ scan for 30 s and the radioactivity concentration in the arterial blood was measured by a Well counter system (Shimadzu Corporation, Kyoto, JAPAN). In order to obtain the AIF, the radioactivity in the arterial blood during a $^{15}O_2$–$C^{15}O_2$ scan was continuously monitored by a GSO detector [17] with a flow rate of 3.5 mL/min. The inner diameter of the tube was approximately 2 mm, and the distance from the catheter to the detector was 20–25 cm.

Residual $C^{15}O$ radioactivity

As described in the "Introduction", the AIF and PET counts obtained during a DARG study may be contaminated by residual $C^{15}O$ radioactivity. By assuming that the $C^{15}O$ was physically decayed but not biologically cleared, the radioactivity of the $C^{15}O$ in the AIF and PET counts during the O_2–CO_2 scan could be quantified. The residual radioactivity of the $C^{15}O$ [$R_{CO}(0)$ (Bq/mL)] in the AIF at the start time of the O_2–CO_2 can be written as follows:

$$R_{\mathrm{CO}} = A_{\mathrm{CO}}\cdot\exp(-\lambda T), \quad (6)$$

where A_{CO} (Bq/mL) is the measured arterial radioactivity for $C^{15}O$ by the Well counter and λ is the physical decay constant for ^{15}O (0.005670 s^{-1}).

PET counts from the residual $C^{15}O$ (C_{CO}) were calculated from R_{CO} and the measured CBV (V_B) by $C^{15}O$ scan from Eq. 2 as follows

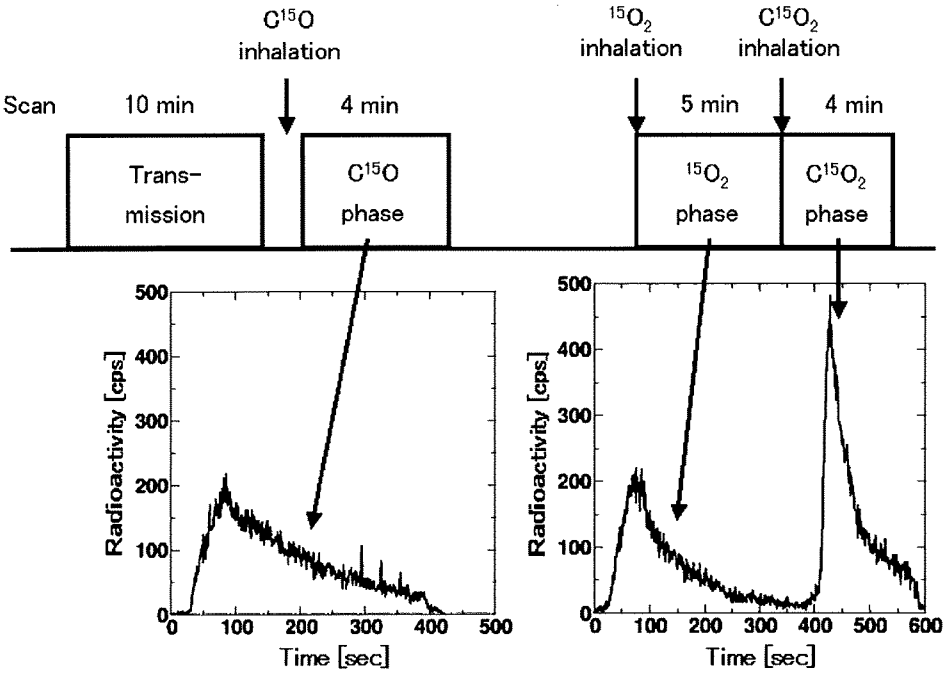

Fig. 1 Schematic diagram of PET study with DARG method protocol. After a 10 min transmission scan, $C^{15}O$ gas is inhaled for 30 s before the start of a 4 min scan. There is approximately 10 min in the administration interval for $C^{15}O$ and $^{15}O_2$. Next, a 9 min single scan with sequential administration of $^{15}O_2$ and $C^{15}O_2$ is performed. The administration interval between $^{15}O_2$ and $C^{15}O_2$ is 300 s. The graphs below are arterial input functions without corrections for decay, delay, and scaling for $C^{15}O$ (*left*), $^{15}O_2$ and $C^{15}O_2$ (*right*)

$$C_{CO} = R_{CO} \cdot \rho_{blood} \cdot \rho_{brain} \cdot R_{Hct} \cdot V_B. \quad (7)$$

We proposed a subtraction method that eliminates the influence of the $C^{15}O$ radioactivity in both the AIF and PET counts during the O_2–CO_2 scan. The true AIF (A_{True}) of the $^{15}O_2$–$C^{15}O_2$ at time t was obtained by subtracting R_{CO} from the measured whole radioactivity [$A_{whole}(t)$], i.e.,

$$A_{True}(t) = A_{Whole}(t) - R_{CO}. \quad (8)$$

Note that $A_{True}(t)$ and $A_{Whole}(t)$ were corrected for the physical decay of ^{15}O against the scan start time 0. PET counts without the residual CO radioactivity could be obtained by subtracting C_{co} in Eq. (7) from the observed PET counts as follows:

$$C_{True}(t) = C_i(t) - C_{co}. \quad (9)$$

Using $A_{True}(t)$ and $C_{True}(t)$, CBF and OEF were calculated in the DARG manner.

Simulation studies

As shown in Eq. 1, DARG calculation does not take into count the residual radioactivity of the CO. However, in an actual situation, both the PET count [Ci(t)] and the input function (A_{O_2} and A_{H_2O}) might contain radioactivity from the $C^{15}O$. So, the CBF and OEF values calculated by the DARG method are influenced by the $C^{15}O$ radioactivity, causing error and noise in the terms of Eq. 1. Computer simulations were performed to evaluate this influence. Both normal and ischemic models were considered in these simulations. Moreover, the effect of the subtraction method was examined.

The simulations were performed using a PC [CPU: Intel (R) Pentium (R) 4 2.80 GHz, OS: Linux Fedora Core 7] with a PyBLD environment [18].

Simulated input function with CO radioactivity

We used a typical arterial input function from one patient's data for the simulations. From the measured input function, the input functions with $C^{15}O$ radioactivity (combined input function, CIF) were generated using Eq. 6. The amount of residual $C^{15}O$ radioactivity was varied by changing two conditions, the time lag between the $C^{15}O$ scan and the $^{15}O_2$–$C^{15}O_2$ scan (T in Eq. 6), and the $C^{15}O$ radioactivity against the $^{15}O_2$ radioactivity (A_{co} in Eq. 6). The time lags selected were 60, 100, 200, 400, and 800 s, and the inhaled $C^{15}O$ radioactivity was either 25% (case '25%') or 100% (case '100%') of the $^{15}O_2$ inhaled radioactivity. 100 sets of noisy arterial TACs for $C^{15}O$ were realized by assuming that the standard deviation of the $C^{15}O$ radioactivity was equal to the square root of the $C^{15}O$ radioactivity. Figure 2 (left) shows the CIF after $^{15}O_2$ gas inhalation in a case where the time lag was 60 s. These TACs did not correct the physiological decay of $^{15}O_2$. For the subtraction method, $A_{True}(t)$ in Eq. 8 was computed for each dataset.

Simulated tissue TAC with CO radioactivity

Using the typical input function and Eq. 1, the tissue TAC during a $^{15}O_2$–$C^{15}O_2$ scan was simulated. We considered two physiological conditions, namely the normal condition

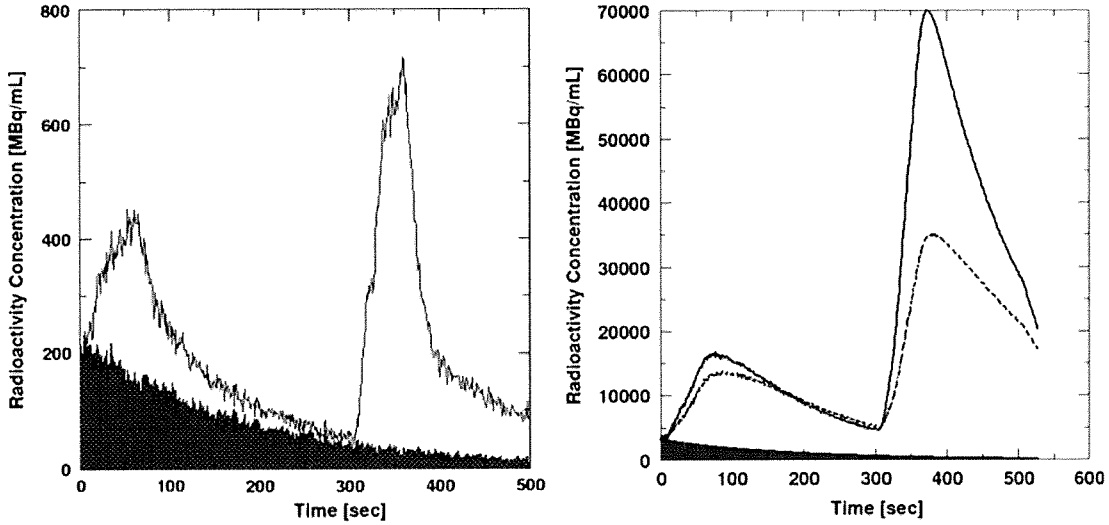

Fig. 2 Input function (*left*) and PET count curves (*right*) during the $^{15}O_2$–$C^{15}O_2$ scan. These curves have the added residual $C^{15}O$ radioactivity (hatched region). The interval time for the $C^{15}O$ and $^{15}O_2$ is 60 s, and the inhaled $C^{15}O$ radioactivity is 100% of the peak value for $^{15}O_2$. $C^{15}O$ time-activity curve. The *solid line* in the *right graph* indicates the PET counts in the normal model, and the *dashed line* is the PET counts in the ischemic model

(CBF = 0.5 mL/g tissue/min, OEF = 0.4, CBV = 0.04, mL/g, p = 0.8 mL/g, Fv = 0.835, and R_{Hct} = 0.85) and an ischemic condition (CBF = 0.2 mL/g tissue/min, OEF = 0.7, CBV = 0.04 mL/g, p = 0.8 mL/g, Fv = 0.835, and R_{Hct} = 0.85). The tissue radioactivity from the residual $C^{15}O$ radioactivity was added to the simulated tissue TACs using Eq. 7. 100 sets of noisy tissue TACs were generated using an NEC model [19]. Figure 2 (right) shows a simulated tissue TAC under the condition of a time lag of 60 s and the case '100%'. For the subtraction method, $C_{True}(t)$ in Eq. 9 was computed for each dataset.

Calculation and evaluation of CBF and OEF values

The $H_2^{15}O$ contents (A_{H_2O}) and $^{15}O_2$ contents (A_{O_2}) were separated from the input functions using the separation method proposed by Kudomi et al. [16]. This separation is demonstrated in Fig. 3. The CBF and OEF values were computed from the A_{H_2O}, A_{O_2}, and the tissue TACs by means of Eqs. 4 and 5. The errors, in the form of bias and coefficient of variance (COV), in the estimated CBF and OEF values were calculated by comparing them with the true CBF and OEF values.

Results

Tables 1 and 2 show the results of the estimated values and COV for CBF and OEF in this simulation study using the conventional DARG method in the cases of the normal model and ischemic model, respectively. As shown in these tables, the estimated CBF and OEF values were underestimated in all cases due to the residual $C^{15}O$ radioactivity. For instance, in the case of the normal model and a time lag of 60 s, the underestimation of the estimated OEF value

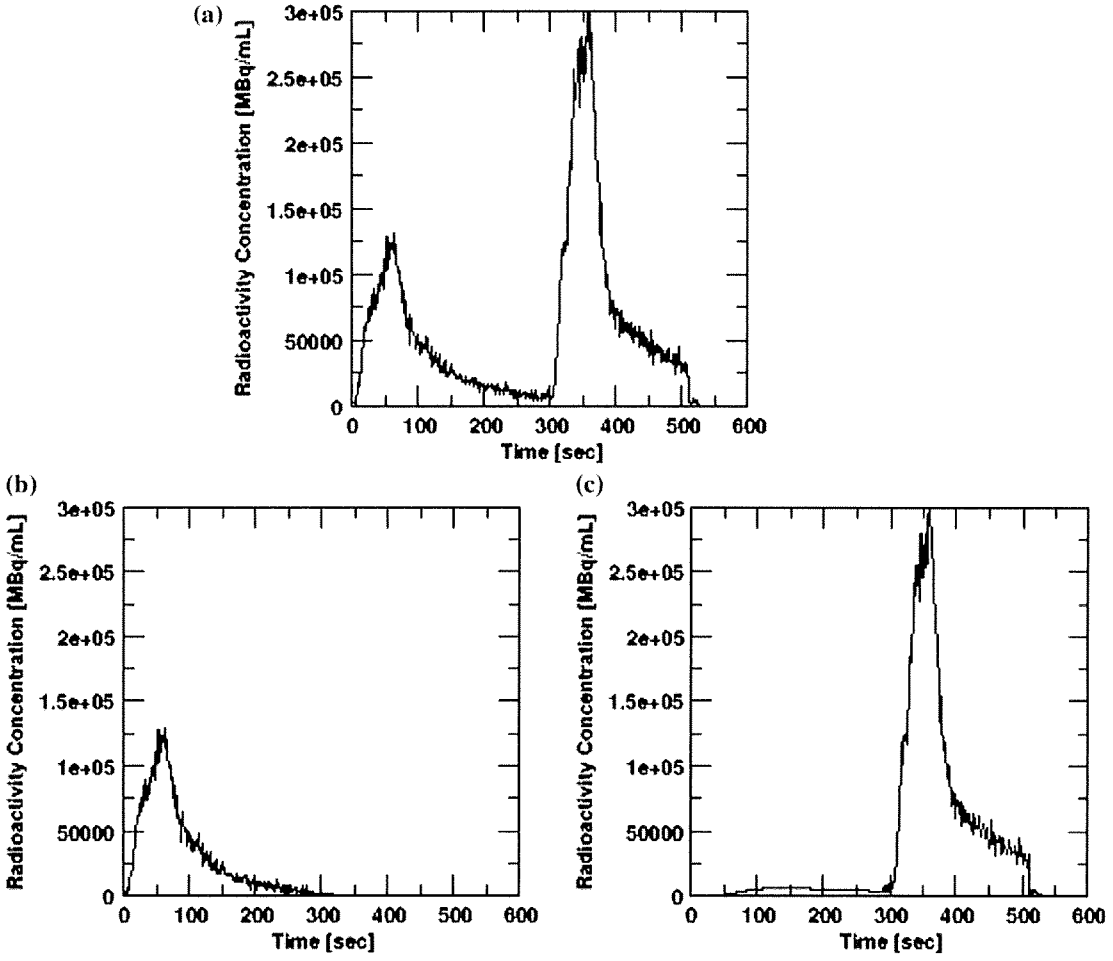

Fig. 3 Separation of the input function for the $^{15}O_2$–$C^{15}O_2$ scan. Total input function (**a**), $^{15}O_2$ input function (**b**), and $C^{15}O_2$ input function (**c**) separated from the total input function. The radioactivity observed earlier than 300 s in the graph (**c**) is the recirculation water

Table 1 Summary of simulation for CBF and OEF in the case '25%' and the case '100%' of the normal model using the conventional DARG method

$C^{15}O$–$^{15}O_2$ time lag (s)	CBF			OEF		
	Average (mL/g/min)	Error (%)	COV (%)	Average	Error (%)	COV (%)
Case '25%'						
60	0.49	−2.06	1.07	0.30	−25.0	1.06
100	0.49	−1.82	0.66	0.31	−21.0	0.52
200	0.50	−0.12	0.23	0.35	−13.5	0.33
400	0.50	−0.04	0.17	0.38	−4.55	0.19
800	0.50	−0.02	0.06	0.40	−0.48	0.07
Case '100%'						
60	0.46	−7.55	1.68	0.16	−60.9	1.64
100	0.47	−6.05	1.37	0.18	−54.4	1.25
200	0.48	−3.91	0.92	0.25	−38.7	0.823
400	0.49	−1.51	0.42	0.34	−16.0	0.45
800	0.50	−0.19	0.08	0.39	−1.90	0.12

Table 2 Summary of simulation for CBF and OEF in the case '25%' and the case '100%' of ischemic model using the conventional DARG method

$C^{15}O$–$^{15}O_2$ time lag (s)	CBF			OEF		
	Average (mL/g/min)	Error (%)	COV (%)	Average	Error (%)	COV (%)
Case '25%'						
60	0.20	−2.72	0.30	0.55	−21.3	0.48
100	0.20	−2.18	0.26	0.58	−17.8	0.37
200	0.20	−1.30	0.17	0.62	−10.9	0.30
400	0.20	−0.45	0.07	0.67	−3.83	0.16
800	0.20	−0.04	0.02	0.70	−0.39	0.06
Case '100%'						
60	0.18	−8.27	0.88	0.33	−52.6	1.08
100	0.19	−6.84	0.71	0.37	−46.9	0.85
200	0.19	−4.43	0.43	0.47	−33.1	0.62
400	0.20	−1.70	0.18	0.61	−13.6	0.36
800	0.20	−0.20	0.04	0.69	−1.60	0.11

was −25% for the case '25%' and −61% for the case '100%'. Larger underestimation values were observed for shorter time lags. The OEF estimation was more sensitive to the residual CO radioactivity than the CBF estimation. Less underestimation was observed in the CBF value in the normal model than in the ischemic model. On the other hand, a larger underestimation was observed in the OEF value in the normal model compared to the ischemic model. The COV was always larger in the normal model than in the ischemic model.

Tables 3 and 4 show the results of the estimated values and the COV for CBF and OEF using the subtraction method. As shown in the tables, no underestimation was observed in all cases. Moreover, the COV values were less than one by the conventional method.

Discussion

CBV images are widely used for the diagnosis of cerebrovascular disease [20]. These images are also utilized to correct the vascular space in the DARG method for CBF and OEF values [15]. Therefore, a $C^{15}O$ scan is mandatory for the DARG protocol. Due to a desire to shorten the total study period, it is often observed that the $^{15}O_2$–$C^{15}O_2$ scan is initiated without waiting long enough for the physical decay of the $C^{15}O$ radioactivity. In this paper, the influences of this residual $C^{15}O$ radioactivity on the CBF and OEF values for the DARG protocol were evaluated by means of computer simulations. According to the results, the CBF and OEF values were underestimated because of the residual $C^{15}O$ radioactivity. The magnitude of the

Table 3 Summary of simulation for CBF and OEF in the case '25%' and the case '100%' of normal model using the DARG method with the subtraction method

$CO–O_2$ time lag (s)	CBF			OEF		
	Average (mL/g/min)	Error (%)	COV (%)	Average	Error (%)	COV (%)
Case '25%'						
60	0.50	0.15	0.37	0.40	−0.17	0.54
100	0.50	0.16	0.33	0.40	−0.18	0.41
200	0.50	0.08	0.27	0.40	−0.31	0.34
400	0.50	−0.04	0.13	0.40	−0.60	0.18
800	0.50	0.02	0.04	0.40	0.12	0.07
Case '100%'						
60	0.50	0.28	0.53	0.40	−0.24	1.02
100	0.50	0.32	0.53	0.40	−0.45	0.97
200	0.50	0.17	0.40	0.40	−0.61	0.70
400	0.50	0.04	0.27	0.40	−0.34	0.41
800	0.50	−0.02	0.07	0.40	−0.17	0.12

Table 4 Summary of simulation for CBF and OEF in the case '25%' and the case '100%' of ischemic model using the DARG method with the subtraction method

$CO–O_2$ time lag (s)	CBF			OEF		
	Average (mL/g/min)	Error (%)	COV (%)	Average	Error (%)	COV (%)
Case '25%'						
60	0.20	0.05	0.15	0.70	−0.13	0.46
100	0.20	0.05	0.14	0.70	−0.14	0.36
200	0.20	0.00	0.11	0.70	−0.25	0.29
400	0.20	−0.05	0.06	0.70	−0.51	0.16
800	0.20	0.01	0.02	0.70	0.11	0.06
Case '100%'						
60	0.20	0.09	0.25	0.70	−0.22	0.86
100	0.20	0.10	0.24	0.70	−0.36	0.83
200	0.20	0.03	0.17	0.70	−0.50	0.62
400	0.20	−0.01	0.11	0.70	−0.27	0.36
800	0.20	−0.02	0.04	0.70	−0.15	0.11

underestimation depended on the amount of $C^{15}O$ radioactivity, the time interval between the $C^{15}O$ scan and the $^{15}O_2$–$C^{15}O_2$ scan, and the disease model we assumed. By subtracting the $C^{15}O$ radioactivity from the input function and PET counts, this underestimation could be eliminated, which resulted in shortening the total study period of the DARG protocol.

Underestimation of CBF and OEF values due to residual $C^{15}O$ radioactivity

In general, overestimations of the arterial radioactivity or PET counts can cause underestimation or overestimation of physiological measures (CBF and OEF), respectively, in the DARG method. Thus, the residual $C^{15}O$ radioactivity might induce the bias in either of direction. As shown in our results, the estimated CBF and OEF values were both underestimated due to the residual $C^{15}O$ radioactivity, which indicates that the bias of the input function by the $C^{15}O$ radioactivity more strongly influenced the estimates than the bias of the PET counts by the $C^{15}O$ radioactivity. In our simulation, the CBV was fixed as 0.04 mL/mL. If the larger CBV was assumed (i.e. dilatation of blood vessel), more residual $C^{15}O$ radioactivity was added on the PET counts and the bias of the total PET counts was increased by Eq. 1, which results in less underestimation for the CBF and OEF values. Note that in this paper, we evaluated not $CMRO_2$ but OEF. $CMRO_2$ is derived by being multiplied CBF and OEF values. Thus, the magnitude of the underestimation in $CMRO_2$ could be larger than those of CBF and OEF.

Tables 1 and 2 suggest that the normal model underestimated OEF more than the ischemic model because of the residual $C^{15}O$ radioactivity. On other hand, the normal

model underestimated CBF less than the ischemic model because of the residual $C^{15}O$ radioactivity. Although the DARG method uses $^{15}O_2$ phase (PET data before the inhalation of $C^{15}O_2$) and $C^{15}O_2$ phase (PET data after the inhalation of $C^{15}O_2$) datasets, and simultaneously estimates CBF and OEF values, the PET data of the $^{15}O_2$ phase were dominant in the determination of OEF and those of the $C^{15}O_2$ phase were dominant in the determination of CBF. As shown in Tables 1 and 2, the amount of the underestimation for OEF is larger than for CBF, which can be explained by the amount of residual $C^{15}O$ radioactivity in both phases. As shown in Fig. 2, the influence of $C^{15}O$ on the input function was much higher in the $^{15}O_2$ phase than in the $C^{15}O_2$ phase. The residual $C^{15}O$ radioactivity led to the underestimation of CBF, mainly determined in the $C^{15}O_2$ phase. However, this underestimation was not enough to explain the bias of the input function in the $^{15}O_2$ phase. The first term on the right side of Eq. 1 has only CBF (f) as a parameter and the value of the first term is much higher in the normal model than in the ischemic model due to the higher CBF of the normal model, which implies that a greater underestimation for OEF could occur in the normal model to compensate for the insufficient underestimation of CBF. The ischemic model has a lower CBF than the normal model, which results in the slow washout of $^{15}O_2$ in tissue (the second term on the right side of Eq. 1). Therefore, the ischemic model has a greater source of underestimation for CBF than the normal model during the $C^{15}O_2$ phase.

As shown in Tables 1, 2, 3, and 4, the COVs of CBF and OEF in the ischemic model were smaller than the COVs in the normal model. The non-linear relationship between the PET counts and CBF attributed to this phenomenon [13]. The PET counts of the normal model were higher than those of the ischemic model, and the higher PET counts emphasized the noise due to this non-linearity.

Our results suggest that attention must be paid to the interpretation of CBF and OEF images from DARG, if contaminated by the significant amount of the residual $C^{15}O$ radioactivity namely: the magnitude of the error may not be uniform across different physiological conditions in the brain.

Subtraction method

The subtraction method successfully eliminated the influence of the $C^{15}O$ radioactivity on both the input function and PET counts during the $^{15}O_2$–$C^{15}O_2$ scan, and no errors in the CBF and OEF values due to the residual $C^{15}O$ radioactivity were observed. In theory, there is no statistical advantage for the subtraction method compared to the conventional method. However, as shown in Tables 3 and 4, the COV by the subtraction method was smaller than the value by the conventional method. It is necessary to separate the $^{15}O_2$ contents and $C^{15}O_2$ contents in the measured input function prior to the DARG calculation. For this separation, we utilized the linear method proposed by Kudomi et al. [16]. The linear method estimates the $^{15}O_2$ contents in the input function after $C^{15}O_2$ inhalation by linear extrapolation. In the conventional method, due to the offset of the input function by the residual $C^{15}O$ radioactivity, the estimated $^{15}O_2$ contents remain until the last in most cases. On other hand, in the subtraction method, by subtracting the $C^{15}O$ radioactivity from the input function, the offset of the input function is removed. Then, in many cases the $^{15}O_2$ contents estimated by the extrapolated line go to zero. This causes a reduction of the variation in the estimated CBF and OEF values compared to the conventional method.

The estimation of the recirculation water in the input function is based on the empirical model [10], and this model may not work owing to the residual $C^{15}O$ radioactivity, which results in biased CBF and OEF values. This bias can be removed by the subtraction method. Thus, by using the subtraction method, accurate CBF and OEF values can be measured no matter how much $C^{15}O$ radioactivity exists, which results in shortening the total PET study. The subtraction method could be applied, not only to the DARG protocol, but also to the conventional ARG and steady-state protocols. In this simulation, we assumed no biological decay of $C^{15}O$, which is not true in the actual data, and the subtraction method might over-subtract the influence of $C^{15}O$ radioactivity. The biological half-life of $C^{15}O$ is difficult to determine within a period of ordinary PET scan owing to the short life of the ^{15}O radionuclide. We tested simulated data with a biological half-life of 10 min, and there were no significant differences in the estimated CBF and OEF values compared to the results shown in this paper. In order to apply the subtraction method in clinical study, further studies are, however, required to verify the influence of biological decay.

Sequence of PET scans

In this paper, the sequence of the scans was a $C^{15}O$ scan followed by a $^{15}O_2$–$C^{15}O_2$ scan. If the $C^{15}O$ scan was performed after the $^{15}O_2$–$C^{15}O_2$ scan, our results were not valid. The reason for this sequence ($C^{15}O$ scan followed by a $^{15}O_2$–$C^{15}O_2$ scan) was to shorten the total duration of the PET study by exchanging the target gas (from N_2 containing O_2 to N_2 containing CO_2) only once (the synthesis of $C^{15}O$ and $^{15}O_2$ shares the same target in a cyclotron but uses different one from that of $C^{15}O_2$). Furthermore, the sequence of $^{15}O_2$–$C^{15}O_2$ produces better results than the sequence of $C^{15}O_2$–$^{15}O_2$ [15]. In order to further shorten the total study time, more development efforts are needed

in relation to the delivery system for the radioactive gases, which should have the ability to deliver such gases quickly.

The results in this paper were based only on the computer simulations. It could be expected to have several difficulties to show validities of our results using actual PET measurements by several reasons such as (1) PET cannot differentiate between photon from residual $C^{15}O$ and photon from either $^{15}O_2$ or $C^{15}O_2$, (2) large inter-subject variation for cerebrovascular disease, (3) large amounts of radiation exposure to patients from $C^{15}O$ in the case of large inhalation of $C^{15}O$. For the validation of our results, PET studies with ischemic animal model will be anticipated.

Conclusions

In this paper, we verified the influence of $C^{15}O$ radioactivity on the computation of CBF and OEF using the DARG protocol. We found that the bias and noise in the CBF and OEF values depended on the amount of residual $C^{15}O$ radioactivity during the scanning for $^{15}O_2$ and $C^{15}O_2$, and on the physiological conditions of the brain tissue. By using the subtraction method, the bias could be eliminated. Finally, we discussed the effects of the recirculation water and the biological decay for $C^{15}O$ radioactivity on the computation of CBF and OEF using the DARG method.

References

1. Frackowiak RS, Jones T, Lenzi GL, Heather JD. Regional cerebral oxygen utilization and blood flow in normal man using oxygen-15 and positron emission tomography. Acta Neurol Scand. 1980;62:336–44.
2. Frackowiak RS, Lenzi GL, Jones T, Heather JD. Quantitative measurement of regional cerebral blood flow and oxygen metabolism in man using 15O and positron emission tomography: theory, procedure, and normal values. J Comput Assist Tomogr. 1980;4:727–36.
3. Mintun MA, Raichle ME, Martin WR, Herscovitch P. Brain oxygen utilization measured with O-15 radiotracers and positron emission tomography. J Nucl Med. 1984;25(2):177–87.
4. Lammertsma AA, Jones T. Correction for the presence of intravascular oxygen-15 in the steady-state technique for measuring regional oxygen extraction ratio in the brain: 1. Description of the method. J Cereb Blood Flow Metab. 1983;3:416–24.
5. Subramanyam R, Alpert NM, Hoop B Jr, Brownell GL, Yaveras JM. A model for regional cerebral oxygen distribution during continuous inhalation of 15O2, C15O, and C15O2. J Nucl Med. 1978;19:48–53.
6. Lammertsma AA, Heather JD, Jones T, Frackowiak RS, Lenzi GL. A statistical study of the steady state technique for measuring regional cerebral blood flow and oxygen utilization using 15O. J Comput Assist Tomog. 1982;6:566–73.
7. Correia JA, Alpert NM, Buxton RB, Ackerman RH. Analysis of some errors in the measurement of oxygen extraction and oxygen consumption by the equilibrium inhalation method. J Cereb Blood Metab. 1985;5:591–9.
8. Okazawa H, Ymauchi H, Sugimoto K, Takahashi M, Toyoda H, Kishibe Y, et al. Quantitative comparison of the bolus and steady-state methods for measurement of cerebral perfusion and oxygen metabolism: positron emission tomography study using 15O-gas and water. J Cereb Blood Metab. 2001;21:793–803.
9. Okazawa H, Ymauchi H, Sugimoto K, Toyoda H, Kishibe Y, Takahashi M. Effects of acetazolamide on cerebral blood flow, blood volume, and oxygen metabolism: a positron emission tomography study with healthy volunteers. J Cereb Blood Flow Metab. 2001;21:1472–9.
10. Iida H, Jones T, Miura S. Modeling approach to eliminate the need to separate arterial plasma in oxygen-15 inhalation positron emission tomography. J Nucl Med. 1993;34:1333–40.
11. Sadato N, Yonekura Y, Senda M, Iwasaki Y, Matoba N, Tamaki N, et al. PET and the autoradiographic method with continuous inhalation of oxygen-15-gas: theoretical analysis and comparison with conventional steady-state methods. J Nucl Med. 1993; 34:1672–80.
12. Hatazawa J, Fujita H, Kanno I, Satoh T, Iida H, Miura S, et al. Regional cerebral blood flow, blood volume, oxygen extraction fraction, and oxygen utilization rate in normal volunteers measured by the autoradiographic technique and the single breath inhalation method. Ann Nucl Med. 1995;9:15–21.
13. Shidahara M, Watabe H, Kim KM, Oka H, Sago M, Hayashi T, et al. Evaluation of a commercial PET tomograph-based system for the quantitative assessment of rCBF, rOEF and rCMRO2 by using sequential administration of ^{15}O-labeled compounds. Ann Nucl Med. 2002;16(5):317–27.
14. Hattori N, Bergsneider M, Wu HM, Glenn TC, Vespa PM, Hovda DA, et al. Accuracy of a method using short inhalation of 15O–O2 for measuring cerebral oxygen extraction fraction with PET in healthy humans. J Nucl Med. 2004;45:765–70.
15. Kudomi N, Hayashi T, Teramoto N, Watabe H, Kawachi N, Ohta Y, et al. Rapid quantitative measurement of $CMRO_2$ and CBF by dual administration ^{15}O-labeled oxygen and water during a single PET scan—a validation study and error analysis in anesthetized monkeys. J Cereb Blood Flow Metab. 2005;25:1209–24.
16. Kudomi N, Watabe H, Hayashi T, Iida H. Separation of input function for rapid measurement of quantitative $CMRO_2$ and CBF in a single PET scan with a dual tracer administration method. Phys Med Biol. 2007;52(7):1893–908.
17. Kudomi N, Choi E, Yamamoto S, Watabe H, Kim KM, Shidahara M, et al. Development of a GSO Detector Assembly for a Continuous Blood Sampling System. IEEE Trans Nucl Sci. 2003; 50(1):70–3.
18. Carson RE. Parameter estimation in positron emission tomography. In: Phelps ME, Mazziotta JC, Schelbert HR, editors. Positron emission tomography and autoradiography. New York: Raven Press; 1986. p. 347–90.
19. Shidahra M, Watabe H, Kim KM, Kudomi N, Ito H, Iida H. Optimal scan time of oxygen-15-labeled gas inhalation autoradiographic method for measurement of cerebral oxygen extraction fraction and cerebral oxygen metabolic rate. Ann Nucl Med. 2008;22(8):667–75.
20. Ito H, Kanno I, Fukuda H. Human cerebral circulation: positron emission tomography studies. Ann Nucl Med. 2005;19(2):65–74.

NeuroImage xxx (2009) xxx–xxx

Contents lists available at ScienceDirect

NeuroImage

journal homepage: www.elsevier.com/locate/ynimg

Quantitative evaluation of changes in binding potential with a simplified reference tissue model and multiple injections of [^{11}C]raclopride

Yoko Ikoma [a,b,*], Hiroshi Watabe [a], Takuya Hayashi [a], Yoshinori Miyake [c], Noboru Teramoto [a], Kotaro Minato [b], Hidehiro Iida [a]

[a] Department of Investigative Radiology, National Cardiovascular Center Research Institute, Suita, Osaka, Japan
[b] Graduate School of Information Science, Nara Institute of Science and Technology, Ikoma, Nara, Japan
[c] Department of Radiology and Nuclear Medicine, National Cardiovascular Center Hospital, Suita, Osaka, Japan

ARTICLE INFO

Article history:
Received 20 February 2009
Revised 27 May 2009
Accepted 29 May 2009
Available online xxxx

Keywords:
Positron emission tomography
[^{11}C]raclopride
Dopamine D_2 receptor
Multiple injections
Binding potential

ABSTRACT

Positron emission tomography (PET) with [^{11}C]raclopride is widely used to investigate temporal changes in the dopamine D_2 receptor system attributed to the dopamine release. The simplified reference tissue model (SRTM) can be used to determine the binding potential (BP_{ND}) value using the time–activity curve (TAC) of the reference region as input function. However, in assessing temporal changes in BP_{ND} using the SRTM, multiple [^{11}C]raclopride PET scans are required, and a second scan must be performed after the disappearance of the [^{11}C]raclopride administered in the first scan. In this study, we have developed an extended multiple-injection SRTM to estimate the BP_{ND} change, from a single PET scan with multiple injections of [^{11}C]raclopride, and we have validated this approach by performing numerous simulations and studies on monkeys. In the computer simulations, TACs were generated for dual injections of [^{11}C]raclopride, in which binding conditions changed during the scans, and the BP_{ND} values before, and after, the second injection were estimated by the proposed method. As a result, the reduction in BP_{ND} was correlated, either with the integral of released dopamine, or with the administered mass of raclopride. This method was applied to studies on monkeys, and was capable of determining two identical BP_{ND} values when there were no changes in binding conditions. The BP_{ND} after the second injection decreased when binding conditions changed due to an increase in administered raclopride. An advantage of the proposed method is the shortened scan period for the quantitative assessment of the BP_{ND} change for neurotransmitter competition studies.

Introduction

Neuroreceptor imaging using positron emission tomography (PET) and [^{11}C]raclopride has made it possible to determine the density of striatal dopamine D_2 receptors *in vivo* (Farde et al., 1985; Köhler et al., 1985; Hall et al., 1988). The binding potential ($BP_{ND} = k_3/k_4$) derived from rate constants in a two-tissue compartment model has been used to quantify the receptor binding (Mintun et al., 1984). Endres et al. then developed an extended compartment model, which included the released neurotransmitter concentration, and demonstrated that [^{11}C]raclopride binding decreased after the administration of amphetamine, which resulted in the displacement of the raclopride due to competition with increased dopamine (Endres et al., 1997, Carson et al., 1997). The model showed that the change in BP_{ND} between the baseline and the stimulated state was related to the total amount of released dopamine. Applying this theory, it has been shown that amphetamine-related reductions in [^{11}C]raclopride-specific binding in patients with schizophrenia was significantly greater than in healthy volunteers (Breier et al., 1997) and that a reduction in [^{11}C]raclopride binding was observed while playing a video game which resulted in the release of endogenous dopamine (Koepp et al., 1998). In this competition paradigm, two PET studies are necessary to measure the BP_{ND} values of the baseline and competed conditions, and a long study period is required.

On the other hand, single-scan studies with bolus-plus-continuous infusion (B/I) of the tracer, applied for the measurement of reduction in BP_{ND} due to an amphetamine challenge, were also performed (Carson et al., 1997, Endres et al., 1997). In these studies, a stimulus was administered during infusion of the tracer, and the change in binding between pre- and post-amphetamine intervention was measured as the tissue-to-plasma concentration ratio at equilibrium. This method enables the direct measurement of receptor-binding

* Corresponding author. Department of Investigative Radiology, National Cardiovascular Center Research Institute, 5-7-1, Fujishirodai, Suita, Osaka, 565-8565, Japan. Fax: +81 6 6835 5429.
E-mail address: ikoma@ri.ncvc.go.jp (Y. Ikoma).

1053-8119/$ – see front matter © 2009 Elsevier Inc. All rights reserved.
doi:10.1016/j.neuroimage.2009.05.099

changes in a single scan. However, the design of the protocol requires that the tracer kinetics attain equilibrium within the measurement period of the pre- and post-amphetamine challenges (Watabe et al., 2000), and dynamic data that does not reach equilibrium may cause systematic errors in the estimates of binding changes (Zhou et al., 2006).

To compute the BP_{ND} value, the simplified reference tissue model (SRTM) is often used. The SRTM can provide the BP_{ND} without invasive arterial blood sampling by using a time–activity curve (TAC) of the reference region where specific bindings are negligible (Lammertsma and Hume, 1996). Recently, an extended simplified reference tissue model (ESRTM) was developed in order to quantify the reduction in BP_{ND} with B/I administration (Zhou et al., 2006). In the ESRTM method, the BP_{ND} of the SRTM was estimated separately, before and after, the pharmacological challenge during a 90 min scan with B/I administration. The group reported that stimulus-induced BP_{ND} changes, obtained from equilibrium analysis in the non-equilibrium state, resulted in an underestimation of the reduction in BP_{ND}, and that this was significantly improved by using the ESRTM. Nonetheless, B/I administration requires the equipment to provide [^{11}C]raclopride constantly during the scan, and there are often technical problems.

Kim et al. (2006) developed a method to measure regional cerebral blood flow in pre- and post-pharmacological stress from a single session of single photon emission computed tomography (SPECT) scanning with dual injections of ^{123}I-iodoamphetamine. In their paper, they showed mathematical derivation for estimating CBF values from two conditions in a single session of SPECT study. By advancing their method, we have developed a method to detect changes in receptor binding using a single session of PET scanning in conjunction with multiple bolus injections of [^{11}C]raclopride synthesized once before the scan (Watabe et al., 2006). In our approach, the SRTM was extended to measure the BP_{ND} of each injection, and we validated this approach by performing numerous simulations and studies on monkeys using PET and [^{11}C]raclopride.

Methods

Theory

The simplified reference tissue model (SRTM) provides BP_{ND} without arterial blood sampling by eliminating the arterial plasma TAC arithmetically from model equations, by using the TAC of the reference region where specific bindings are negligible. The radioactivity concentration of the target region (C_t) is expressed as Eq. (1), using the radioactivity concentration in the reference region (C_r), under the assumption that the target and reference regions can be expressed using the one-tissue compartment model and that the ratios of K_1 and k_2 are equal between the target and reference regions (Lammertsma and Hume, 1996).

$$C_t(t) = R_1 C_r(t) + \left(k_2 - \frac{R_1 k_2}{1 + BP_{ND}}\right) e^{-\frac{k_2}{1+BP_{ND}}t} \otimes C_r(t) \quad R_1 = K_1 / K_1^r \tag{1}$$

where K_1 and k_2 are the rate constants for the transfer from plasma to the displaceable compartment in the target tissue and from the displaceable compartment to plasma, respectively, and K_1^r is the rate constant for the transfer from plasma to the reference tissue.

We have extended this SRTM to a multiple-injection study. In this approach, the first injection of the radioligand was performed at the time of the scan start, and the BP_{ND} was measured as a baseline. Next, a second injection was performed simultaneously with a change in binding conditions, and the BP_{ND} was measured as a competitive state after the second injection. The BP_{ND} values before, and after, the second injection, were estimated by the multiple-injection simplified reference tissue model (MI-SRTM) expressed as follows:

$$\begin{aligned} C_{t1}(t) &= R_{11} C_{r1}(t) + \left(k_{21} - \frac{R_{11} k_{21}}{1 + BP_{ND1}}\right) e^{-\frac{k_{21}}{1+BP_{ND1}}t} \otimes C_{r1}(t) \\ C_{t2}(t) &= R_{12} C_{r2}(t) + \left(k_{22} - \frac{R_{12} k_{22}}{1 + BP_{ND2}}\right) e^{-\frac{k_{22}}{1+BP_{ND2}}t} \otimes C_{r2}(t) \\ &\quad + (C_{t0} - R_{12} C_{r0}) e^{-\frac{k_{22}}{1+BP_{ND2}}t} \end{aligned} \tag{2}$$

where C_{t1} and C_{t2} are the radioactivity concentrations in the target tissue and C_{r1} and C_{r2} are the radioactivity concentrations in the reference tissue for the first and second injections, respectively; t is the time from the first or second injection; C_{t0} and C_{r0} are the radioactivity concentrations of the target and reference tissues at the time of the second injection, respectively.

Firstly, R_{11}, k_{21} and BP_{ND1} were estimated by nonlinear least squares fitting with the iteration of the Gauss–Newton algorithm using data points before the second injection. Next, C_{r0} was calculated by the interpolation of the measured reference TAC, and C_{t0} was estimated using Eq. (1) with estimated R_{11}, k_{21} and BP_{ND1} values. Finally, R_{12}, k_{22}, and BP_{ND2} were estimated by nonlinear least squares fitting using these C_{r0} and C_{t0} values with Eq. (2). In this study using [^{11}C]raclopride, the TAC of the cerebellum was used as a reference TAC.

The present method can be used to generate voxel-based parametric maps. In the voxel-based estimation for parametric imaging of ligand–receptor binding, R_{11}, k_{21} and BP_{ND1} from the first injection and R_{12}, k_{22}, and BP_{ND2} from the second injection in Eq. (2), were estimated by a basis function method in which the model Eq. (2) is solved using linear least squares for a set of basis functions, which enables the incorporation of parameter bounds (Gunn et al., 1997).

Simulation analysis

Three simulation studies were carried out to validate the present approach and to determine: 1) whether the change in BP_{ND} caused by competition to receptor binding could be detected by the MI-SRTM; 2) how would the time delay between the endogenous dopamine release and [^{11}C]raclopride injection affect BP_{ND} estimates, and 3) what was an optimal scan duration for a reliable BP_{ND} estimation?

Detection of BP_{ND} change with dual injections

The MI-SRTM assumes that BP_{ND} alters promptly from BP_{ND1} to BP_{ND2} at the time of the second injection and then remains constant. However, in reality this is unlikely and the binding condition of [^{11}C]raclopride may be continuously changed along time. In this simulation, the detectability of the reduction of BP_{ND} due to changes in binding conditions was investigated. Noiseless time–activity curves of the striatum and cerebellum were generated with a measured plasma TAC and assumed parameter values derived from measurements taken from the monkey study. A TAC of the cerebellum was simulated with a conventional two-tissue compartment, four-parameter model with assumed parameter values obtained previously in our monkey study: $K_1 = 0.034$, $K_1/k_2 = 0.36$, $k_3 = 0.022$, $k_4 = 0.034$. Meanwhile, a TAC of the striatum was simulated with an extended two-tissue compartment model

Please cite this article as: Ikoma, Y., et al., Quantitative evaluation of changes in binding potential with a simplified reference tissue model and multiple injections of [^{11}C]raclopride, NeuroImage (2009), doi:10.1016/j.neuroimage.2009.05.099

expressed as Eq. (3) by the fourth-order Runge–Kutta method (Endres et al., 1997).

$$\begin{aligned}
\frac{dC_f}{dt} &= K_1 C_p(t) - (k_2 + k'_3(t))C_f(t) + k_4 C_b(t) \\
\frac{dC_b}{dt} &= k'_3(t)C_f(t) - k_4 C_b(t) \\
k'_3(t) &= k_{on}\frac{B_{max} - \frac{C_b(t)}{SA}}{1 + D(t)} \\
D(t) &= B_1 \qquad (t<t_2) \\
&= B_2 + A \cdot \exp(-R(t - t_2)) \quad (t \geq t_2)
\end{aligned} \tag{3}$$

where C_f and C_b are the concentrations of radioactivity for free and specifically bound [^{11}C]raclopride in tissue, respectively; B_{max} is the total dopamine D_2 receptor concentration; k_{on} is the bimolecular association rate constant for raclopride; SA is the specific activity of administered [^{11}C]raclopride; D is the concentration of free dopamine. In this simulation study, t_2 was set to 30 min, and SA that was decay corrected to the first injection time was assumed to be equal in first and second injections with a single synthesis. Each assumed parameter for K_1 to k_4 was obtained from our monkey study, and the B_{max} value was as reported previously (Endres et al., 1997), thus $K_1 = 0.033$, $K_1/k_2 = 0.59$, $k_{on} = 0.0048$, $B_{max} = 17.6$; $k_4 = 0.026$; $B_1 = B_2 = 0$, and SA = 37 GBq/μmol at the time of first injection.

First, the magnitude of the BP_{ND} change, derived from an increase in released dopamine, was investigated. Time–activity curves, including dopamine release, were simulated from Eq. (3), in which A varied: 0.5, 1.0, 1.5 and 2.0, and R varied: 0.04, 0.07, and 0.1. In these simulated TACs, BP_{ND1} and BP_{ND2} were estimated by the MI-SRTM, and the relationship between the magnitude of the BP reduction ($\Delta BP = (BP_{ND1} - BP_{ND2})/BP_{ND1}$) and the integral of the dopamine pulse D in Eq. (3) was examined.

Next, the BP change caused by an increase in administered raclopride was investigated. $D(t)$ in Eq. (3) was set to 0, and tissue TACs were generated using the input plasma TAC in which administration of the first injection was assumed as 1 nmol raclopride, and the second injection was amplified from 1 to 50 times greater than the first injection. In these simulated TACs, BP_{ND1} and BP_{ND2} were estimated by the MI-SRTM, and the relationship between the magnitude of ΔBP and the amount of raclopride administered by the second injection was examined.

Effect of binding change timing on BP_{ND} estimates

It is possible that the change in BP_{ND} occurs either before, or after, the second injection of [^{11}C]raclopride. In the MI-SRTM, the error in the estimates for the first injection of [^{11}C]raclopride amplifies the errors in the estimates for the second injection. In this simulation, the effect of the onset of the dopamine pulse on the binding change of BP_{ND}, estimated by the MI-SRTM, was investigated using noiseless simulated TACs. First, TACs with a released dopamine pulse were generated using Eq. (3), with the parameters mentioned above, and three types of pulse ($A = 0.5$, $R = 0.1$; $A = 1.0$, $R = 0.07$; $A = 1.5$, $R = 0.04$) in which the onset time of the dopamine pulse, t_2 in Eq. (3), was changed from −10, −5, 0, 5, 10, 15 min against 30 min intervals of the second injection. The values for BP_{ND1}, BP_{ND2}, and ΔBP were estimated by the MI-SRTM, and the relationship between the onset time of the dopamine pulse and the BP_{ND} estimates was investigated.

Next, TACs were generated by the SRTM with measured cerebellum TACs and assumed parameter values ($R_1 = 0.86$, $k_2 = 0.091$, and $BP_{ND1} = 2.2$) using the fourth-order Runge–Kutta method, assuming a prompt change of BP_{ND} at −10, −5, 0, 5 and 10 min after the second injection (30 min intervals). The value of BP_{ND2} was also varied so that ΔBP would be 0, 10, 20, 30, 40, 50, 60, 70, and 80%. In these simulated TACs, BP_{ND1}, BP_{ND2}, and ΔBP were estimated by the MI-SRTM, and the estimated values were compared with the true values.

Effect of injection interval on BP_{ND} estimates

The relationship between the reliability of the BP_{ND} estimates from the MI-SRTM and the injection interval was investigated with noise-added TACs. A dynamic tracer concentration for [^{11}C]raclopride was derived from the equation of MI-SRTM (Eq. (2)) with a measured cerebellum TAC used as the input function and the rate constant values given as true values ($R_1 = 0.95$, $k_2 = 0.067$, $BP_{ND1} = 2.6$, $BP_{ND2} = 2.6$, 1.8, or 0.78) assuming a prompt BP reduction at the time of the second injection. The timing of the second injection was varied from 20 min to 90 min after the first scan.

The Gaussian-distributed mean-zero noise with variance proportional to the true count was added to the non-decaying tissue activity for each frame using Eq. (4) (Logan et al., 2001):

$$\sigma_i(\%) = 100 \cdot F / \sqrt{C_t(t_i) \cdot e^{-\lambda t_i} \cdot \Delta t_i} \tag{4}$$

where i is the frame number; C_t is the non-decaying tissue radioactivity concentration derived from the rate constants and the input function; t_i is the midpoint time of the i'th frame; Δt_i is the data collection time; λ is the radioisotope decay constant; F is a scaling factor representing the sensitivity of the measurement system, introduced here to adjust the noise level. It should be noted that this equation assumes that noise, which is added to the TAC, is determined by the count of the curve itself. In fact, noise is determined by the total counts in the slice, and is affected by random counts, dead time, etc. In this simulation study, F was set to 15.0 so that the noise level would be the same as the noise level for regions of interest (ROI)-based analysis, and 1000 noisy data sets were generated for each injection interval.

In these simulated TACs, BP_{ND1} and BP_{ND2} were estimated by the MI-SRTM, and estimated BP_{ND1}, BP_{ND2}, and ΔBP values were compared with the true values. Parameter estimates were considered outliers if either BP_{ND1} or BP_{ND2} was outside the range $0.0 < BP_{ND} < 10.0$. The reliability of the estimated parameters was evaluated by the mean and coefficient of variation (COV; SD/mean[%]) of the estimates excluding outliers, and the relationship between the reliability of the parameter estimates and the injection interval was investigated.

Monkey study analysis

Studies on monkeys with dual injections of [^{11}C]raclopride were performed to determine whether the present approach can estimate two identical BP_{ND} values when there is no change in binding conditions during the scan, and whether this approach can detect a change in BP_{ND} values when the binding conditions do change during the scan. The monkeys were maintained and handled in accordance with guidelines for animal research on Human Care and Use of Laboratory Animals (Rockville, National Institute of Health/Office for Protection from Research Risks, 1996). The study protocol was approved by the Subcommittee for Laboratory Animal Welfare of the National Cardiovascular Center.

First, PET studies were performed in four cynomolgus macaques (weight 3.6 ± 0.56 kg) by administering the same molar amount of [^{11}C]raclopride for the first and second injections (Table 1). Anesthesia was induced with ketamine (8.4 mg/kg, intramuscularly) and xylazine (1.7 mg/kg, intramuscularly) and maintained by intravenous propofol (6 mg/kg/h) and vecuronium (0.02 mg/kg/h) during the scan. Initially, 418 ± 111 MBq of [^{11}C]raclopride was administered by a bolus injection, and after 30 min, the same molar amount of [^{11}C]raclopride as for the first injection, was administered by a bolus

Please cite this article as: Ikoma, Y., et al., Quantitative evaluation of changes in binding potential with a simplified reference tissue model and multiple injections of [^{11}C]raclopride, NeuroImage (2009), doi:10.1016/j.neuroimage.2009.05.099